UNIVERSITÀ DEGLI STUDI DI PADOVA

DIPARTIMENTO DI INGEGNERIA INDUSTRIALE

Laurea Magistrale in Ingegneria Aerospaziale

Development of a nanosatellite payload for orbit and attitude determination through laser ranging

Relatore:

Prof: Alessandro Francesconi

Candidato:

Leonardo Brunettin

2026791

Contents

Abstract

Alba CubeSat UniPD is a student project with the goal of designing, building, and launching a 2U CubeSat satellite as part of the ESA "Fly Your Satellite!" programme. One of the objectives of the AlbaSat mission is to determine the satellite's orbit and attitude using laser ranging, which involves illuminating the satellite with a laser beam during its pass over the ground station. The laser beam is reflected by the satellite using Corner Cube Retroreflectors (CCR), which bounce it back to the ground station where it is detected by a telescope. By measuring the time it takes for the laser to return to the ground station, the satellite's position can be precisely estimated. This thesis shows the development process of the AlbaSat payload that enables the aforementioned objective to be achieved. The work was carried out by starting from the project requirements and then conducting a series of analyses to get to a design that complies with those requirements. Subsequently, a commercially available product that reflects the design was chosen through a trade-off analysis. The output of this project phase and of this thesis is a development model that represents the dimensional characteristics of the payload.

Introduction

With recent advancements in miniature space technology, a greater number of smaller low-cost satellites are launched into the LEO for various purposes. The rise of CubeSats, small spacecraft with standardized dimensions of 10cm x 10cm x 10cm (1U), has opened up new opportunities for student teams to participate in space exploration and research. CubeSats are affordable, easily customizable, and can be launched as secondary payloads on larger rockets. As a result, many universities and colleges have established CubeSat programs to provide hands-on experience in spacecraft design, fabrication, and mission operations to their students.

The need for precise orbit determination (POD) has grown significantly due to the increased amount of space-based activities appearing at an accelerating pace. POD has a positive contribution in achieving the requirements of Low-Earth Orbit (LEO) satellite mission which includes improved reliability and continuity. For nearly three decades Satellite Laser Ranging (SLR) has been the primary tracking data for numerous high-profile geodetic satellites such as LAGEOS and TOPEX/-Poseidon. Significant advances in the Global Navigation Satellite System (GNSS), and GNSS data processing algorithms and data distribution, have positioned this technology as the primary tracking technique to support POD in the new era of geodetic satellites. GNSS receivers are nowadays relatively cheap and miniaturized components readily available. With this development, the role of SLR in POD has changed, but it continues to fulfill an essential role. Experience with CHAMP and Jason-1 POD has demonstrated that the SLR tracking is an invaluable tool in the calibration and validation of the GPS orbit solutions. The unambiguous, direct ranges obtained from SLR systems provide a high-accuracy (i.e., sub-cm level) absolute observation of the orbit [1].

1.1 Alba Cubesat UniPD project

Founded in 2019, Alba Cubesat UniPD is a student team from University of Padova aiming to design, build and launch a CubeSat. The team consists of undergraduate and graduate students from various engineering disciplines, including aerospace, mechanical, electrical, and software engineering. The main objective of the project is educational, as students are making experience with hands-on activities, learning about european aerospace industry standards and the design process of a real satellite.
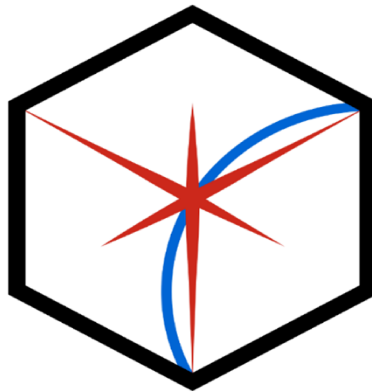

Figure 1.1: Alba CubeSat UniPD logo.

The team is led by the project manager, who oversees the overall project and ensures that members stay on track with goals and timelines. The project manager is supported by system engineers who are responsible for overseeing the design and integration of the various subsystems, ensuring that the CubeSat meets the mission requirements and functions as intended. Each subsystem has a dedicated team with members working together on its development. In addition to these technical roles, there are team members responsible for outreach and education who have been working to promote the project and engage with the broader community. Overall, the team structure of Alba Cubesat UniPD is designed to maximize collaboration and ensure that all aspects of the project are covered.

1.1.1 Mission statement and objectives

The proposed mission has four independent objectives: (1) to collect in-situ measurements of the sub-mm space debris environment in LEO, (2) to study the micro-vibration environment on the satellite throughout different mission phases, (3) to do orbit and attitude determination through laser ranging; (4) to investigate alternative systems for possible Satellite Quantum Communication applications on nanosatellites. The data collected by these technical experiments will enrich the current knowledge of the space environment and will support the research activities currently carried out within the University of Padova.
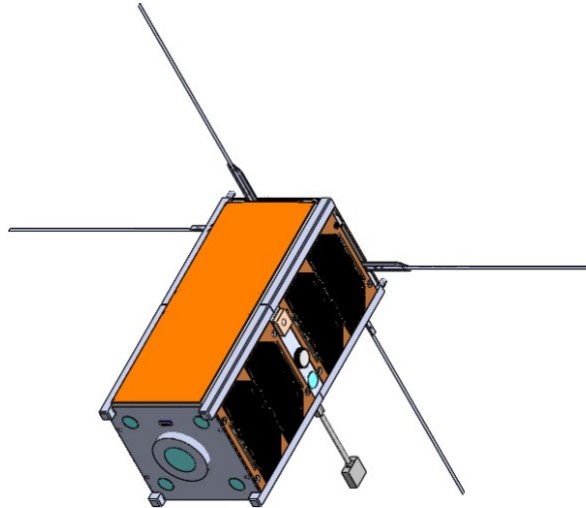
Figure 1.2: Isometric view of AlbaSat in a deployed configuration.

In order to achieve the proposed mission objectives, the team is developing Al-baSat, a 2U CubeSat built mostly from Commercial Off The Shelf (COTS) com-ponents. This ensures lower costs and greater compatibility. Some parts have to be designed from scratch (e.g. some payloads) but the objective is keeping custom parts to a minimum.

1.1.2 Payloads

AlbaSat is equipped with four payloads:

- **Impact sensor**: The aim of the payload is to collect in-situ measurements of the sub-mm space debris environment in LEO. It consists of a series of conductive stripes arranged on a thin nonconductive film and exposed to the space environment. An impact is detected when one or more stripes are severed.

- **Micro-vibration sensor**: The main purpose of this payload is to provide information about the micro-vibrations acting on the CubeSat throughout all mission phases. The payload consists in a triaxial accelerometer, which shall be able to detect the amplitudes of the micro-vibrations for each axis in a 0.1-150 Hz bandwidth.

- **CCR payload**: The CubeSat will be equipped with Corner Cube Retrore-flectors (CCRs) to allow precise orbit and attitude determination through laser ranging from the ground. The CCR reflects a laser beam coming from a ground station allowing to perform time of flight measurements to determine the satel-lite range. The development process of this payload is the main topic of Chapter 3.

- **Quantum Future payload**: The main goal of the Quantum Future Payload (QPL) is to create a new method to test optical receiver for quantum communi-cation such as QGS. The payload is currently being developed by the Quantum Future team to be integrated on AlbaSat.

1.1.3   Subsystems and teams

In addition to the payloads, AlbaSat is composed of various subsystems that guarantee the system functionality and ensure mission success. Each subsystem team is responsible for a specific aspect of the CubeSat, and the success of the project depends on the effective coordination of these teams. Here is a brief description of the technical function of each subsystem team involved in a CubeSat project:

- **Attitude Determination and Control System (ADCS)**: The ADCS team is responsible for designing, integrating, and testing the CubeSat's attitude control system, which may include reaction wheels, magnetorquers, and thrusters. They also develop and test the attitude determination algorithms, which use sensors such as sun sensors, magnetometers, and gyros to calculate the CubeSat's orientation in space.

- **Operations (OPS)**: The OPS team is responsible for developing and testing the CubeSat's operational procedures and modes, which define how the CubeSat will operate during the mission. They also develop and test the CubeSat's mission timeline, which outlines the sequence of events during the mission and ensures that all the subsystems are operated efficiently.

- **Mission Analysis (MA)**: The MA team is responsible for analyzing the feasibility of the mission, the candidate orbits and the expected mission duration. They use orbital simulations including perturbations to assess reentry time and the influence of the space environment on mission duration. They are also responsible of complying with debris mitigation policies and reentry safety.

- **Thermal Control (TCS)**: The TCS team is responsible for designing and testing the CubeSat's thermal control system, which may include passive and active cooling methods such as heat pipes, thermal blankets, and heaters. They use thermal analysis tools and techniques to optimize the thermal performance of the CubeSat and to ensure that the electronic components operate within their temperature range.

- **Electrical Power System (EPS)**: The EPS team is responsible for designing and testing the CubeSat's power system, which may include solar panels, batteries, and power management circuits. They use power analysis tools and techniques to optimize the power budget of the CubeSat and to ensure that all subsystems are powered adequately.

- **Ground Segment (GS)**: The GS team is responsible for designing and testing the CubeSat's communication system, which may include radio transmitters and receivers, antennas, and ground station software. They use communication analysis tools and techniques to optimize the communication link between the CubeSat and the ground station, and to ensure that the CubeSat can transmit and receive data reliably.

- **On-Board Computer (OBC)**: The OBC team is responsible for designing and testing the CubeSat's on-board computer, which controls most of the CubeSat's subsystems. They use software engineering methodologies to develop the

CubeSat's software architecture and to implement the CubeSat's control algorithms. They also develop and test the CubeSat's fault protection and recovery procedures.

- **Structure and Mechanisms (ST&M)**: The ST&M team is responsible for providing the support and protection required for the CubeSat's electronic components, and for designing and testing the CubeSat's deployable structures and mechanisms. They use mechanical engineering tools and techniques to optimize the CubeSat's structural integrity and to ensure that the CubeSat can survive the launch and the harsh space environment.

- **Telemetry Tracking and Control (TT&C)**: The TT&C team is responsible for designing and testing the CubeSat's telemetry, tracking, and control system, which may include radio links and ground station software. They use tracking and control analysis tools and techniques to optimize the CubeSat's orbit and attitude, and to ensure that the CubeSat can be monitored and controlled from the ground station.

1.2 ESA Flight Your Satellite!

ESA's "Fly Your Satellite!" (FYS) programme is a recurring, hands-on programme designed and managed by the ESA Education Office in close collaboration with Universities from ESA Member States, with the objective to complement academic education and inspire, engage, and better prepare students for a more effective introduction to their future professions in the space sector. During the course of the programme, the student teams are supported in the development of their CubeSats, whose mission is conceived at their own universities, and whose development is funded by the universities themselves and/or other national contributors. Coordinated and guided by their professors, the student teams are supported and mentored by ESA specialists through different programme phases, all aiming at ensuring the satellites undergo accurate verification before being offered a chance to fly to space [2].

Figure 1.3: Fly Your Satellite! logo.

During the pandemic, "Fly Your Satellite!" was put on hold, as other student programs by ESA. Alba CubeSat was aiming to propose for the 2020 edition, but the team had to wait until late 2022, when a new opportunity arose as ESA unveiled their new "Fly Your Satellite! Design Booster" programme.

1.2.1 Design Booster pilot edition

ESA's "Fly Your Satellite! Design Booster" is aimed at students working in the design of a CubeSat mission. The programme phases are adapted from the typical development cycle of space missions to fit the context of university projects. The pilot programme follows a fixed schedule spanning 1.5 years. The objective is to help student teams to get from a preliminary design phase to a final design ready for a "Fly Your Satellite!" proposal. Alba CubeSat team was in a good position to propose for Design Booster, as the first iteration of the preliminary design was being concluded.

A number of members of teams attended the FYS Design Booster Training Week at the end of 2022, where they attended training offered by ESA experts. They received valuable pointers, covering different areas such as engineering (design, tests, operations), project management, space debris, and more. About one month after this training, teams defended their CubeSat design in front of a Panel of ESA experts at a Selection Workshop. Selected applicants enterd FYS Design Booster.

Alba CubeSat's proposal was accepted and the team was included among with 5 other teams from various european countries in the pilot edition of Design Booster [3]. From there, the team was assigned two ESA experts to help through the design process, giving precious advice and a schedule with various deadlines, reviews and periodical meetings. The team's job is to deliver a number of documents which will undergo two major reviews from ESA's CubeSat team experts [4].

Based on the design documentation a Baseline Design Review was be conducted, which is a simplified version of the standard ESA review. The overall status of each

CubeSat will be assessed, and with the support of ESA specialists, who identify key issues and assist in solving them, corrective actions are defined and agreed to address the discrepancies identified.
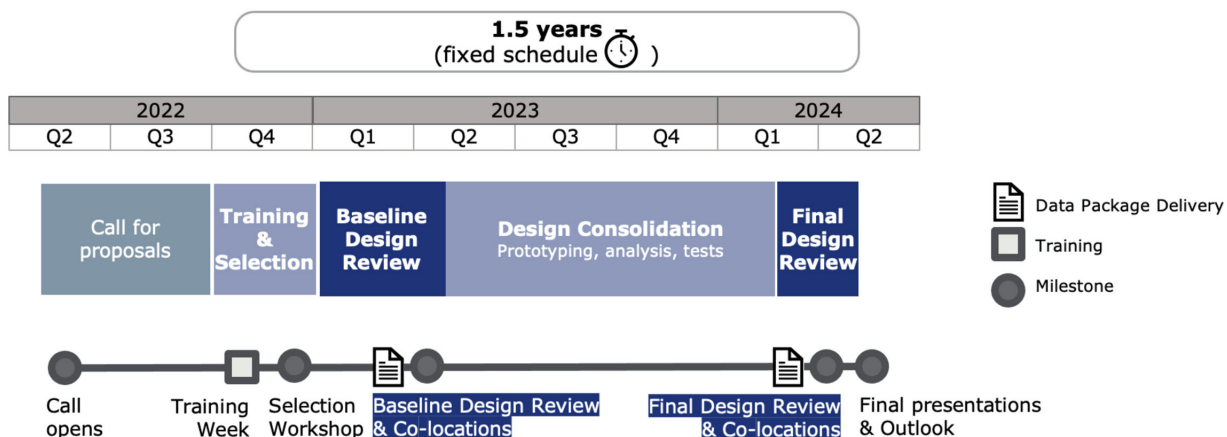

Figure 1.4: Design Booster major milestones.

The output of the reviews is a series of RID (Review Item Discrepancy) which represent a point of concern from the experts on a given part of the design or an analysis. The RIDs are discussed in a series of meetings, from which a number of actions for the team are assigned. For each action a short o long deadline is issued and the team has to adjust the design or the analyses to produce a new version of the documentation addressing the actions. The analyses shown in Chapter 3 have already undergo the Baseline Design Review and have been modified to address all actions opened for the short deadline set for 9th June 2023. All modifications in response to actions have been reviewed and accepted.

Once the Baseline Design Review is concluded, teams will have about one year to consolidate their detailed design. During this period, teams are expected to finalise system and subsystem analysis, develop and test prototypes to increase confidence in the design and -resources and schedule permitting- conduct an environmental test campaign of one of the CubeSat units at the CubeSat Support Facility in ESEC (Belgium).

The programme will conclude with a Final Design Review, scheduled for March-April 2024, a thorough overall examination of the technical and development status of the CubeSat project to check if the detailed design has been consolidated. This practice is tailored from professional space programmes and aims to get students acquainted with ESA and space industry working methodologies and standards. At the end of this process, participating student teams will present their results, the project outlook and lessons learned.

Satellite Laser Ranging

Satellite laser ranging (SLR) is a technique for measuring the precise orbits of satellites using laser pulses. SLR has been used for decades to study the Earth's environment, geodesy, and fundamental physics. This chapter presents a brief literature review of SLR, organized by topic.

The first section provides an overview of the technical aspects of SLR, including the laser ranging process and the instrumentation used. The following section discusses the International Laser Ranging Service (ILRS), which is a global network of SLR stations that provides high-precision measurements of satellite orbits and Earth gravity field. This section describes the history and organization of the ILRS, as well as its role in promoting international collaboration and standardization in SLR research.

The third section focuses on the corner cube retroreflectors, which are the only components of SLR targets placed on satellites discussing the design and properties of corner cubes, as well as their role in achieving SLR measurements.

The fourth section explores the developments in SLR technology that have enabled millimeter-level accuracy in satellite orbit determination describing the techniques and technologies that have contributed to this improvement, such as tracking mount control and laser repetition rate. Finally, the fifth section discusses the use of SLR for attitude determination describing the challenges and techniques.

2.1 Technology overview

The basic principle of SLR is to transmit a laser pulse from a ground-based station to a retroreflector on a satellite, tracked by an optical telescope which has a sensitive light detector at its receiving end. The departing laser pulses trigger an interval counter at a certain time (epoch of data); the laser pulses are reflected and the received laser light pulses are registered by a sensitive light-detecting device. The detector permits a stop signal to be sent to the interval counter. Utilising these round-trip time intervals (time-of-flight) and the speed of light, the range is half of this two-way range [5].

To achieve such high accuracy, SLR systems use specialized instrumentation and data analysis techniques. The laser transmitters used in SLR systems typically produce short pulses of light with a wavelength of 532 nm (green) or 1064 nm (infrared) [6]. The laser pulses are directed towards the satellite using a telescope, and the reflected pulses are collected by a detector located at the ground station. The detector produces an electrical signal that is used to determine the time of flight of the laser pulse.

The core element of a laser ranging system is the high energy laser. The laser is characterized by the high coherence, high degree of collimation of the beam, and the high power density. Therefore, these very high-energy, sharply defined pulses can be transported over large distances. Nowadays, only laser systems of third generation are in use.
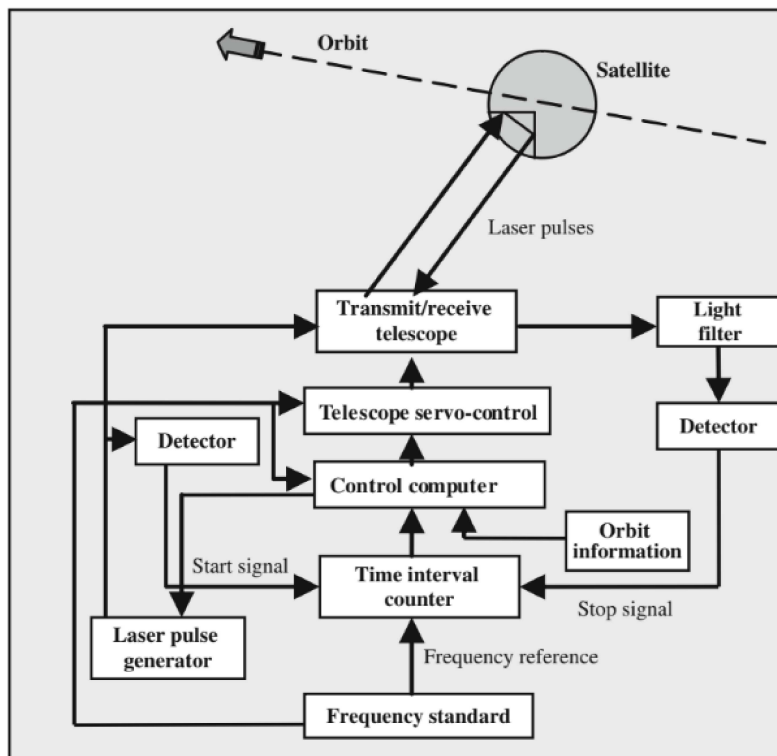

Figure 2.1: Functional schematics of SLR.

9

The retroreflectors on the satellite are the key components that allow for high-precision measurements in SLR. Retroreflectors are typically made of small, highly reflective corner cubes that are arranged in a precise geometric pattern. When a laser pulse hits a corner cube, it is reflected back towards the source with very little scattering or diffraction. This allows for the precise measurement of the time of flight of the laser pulse.

State-of-the-art timers are essential for the SLR technique, since the laser pulses travel with the speed of light, and thus, the error of 1 ns (=1000 ps) would imply an error of 300 mm by means of double travel time. Two timing methods are currently in use: the interval counter and the event timer. Time interval counters measure the time-of-flight of the laser pulse, whereas event timers calculate this value by differencing the laser fire epoch and the pulse reception epoch. Interval timers have the resolution up to 10 ps, but with the advent of kHz laser systems the event timers are largely used due to the need to handle multiple laser shots in flight. Event Timers have nowadays the resolution even of 0.5 ps with 3 ps jitters and 12 kHz repetition rates (3 ps corresponds to 0.9 mm by means of light travel or to 0.45 mm for two-way ranging).

To detect a return signal of a few or single photons from satellites, stations use either a micro-channel plate (MCP) or an avalanche diode, typically a single photon avalanche diode (SPAD). MCP detectors have jitter levels at around 100 ps with far less dark noise than SPAD of around 30-300 Hz and the efficiency level reaching 40%. The SPAD detectors are effective and widely used. The SPAD detectors exhibit an error dependence on incident signal intensity, termed "time-walk". The latest SPAD is designed for kHz operations and has the "dark" noise at the level of 200-300 kHz and the ability to detect single photon events. The typical SPAD detectors have detection fall times of less than 200 ps, quantum efficiencies of >20% and detection jitter of 20-100 ps. In order to perform daytime SLR observations, sophisticated bandwidth filters are required to handle the large noise ratios. Optics with laser wavelength specific transmission bands of typically 0.3 nm are introduced with a "blocking filter" in front of the detector. Some filters are oven controlled and tuned to the desired wavelength.
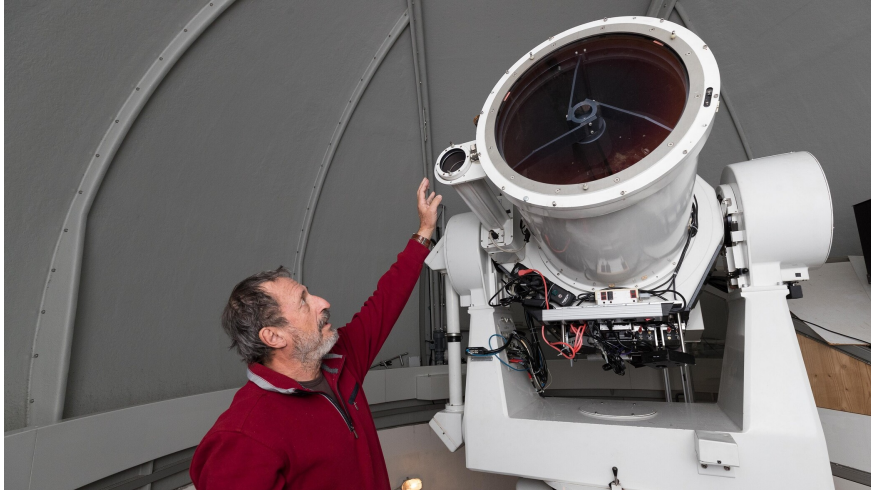
Figure 2.2: SLR telescope in Graz, Austria.

SLR measurements are also affected by various sources of noise and error, such as atmospheric turbulence, satellite motion, and instrument noise. To mitigate these effects, SLR systems employ various data analysis techniques, such as filtering, modeling, and error estimation. Additionally, multiple ground-based stations are used to improve the accuracy and precision of the measurements.

SLR allowed defining a global terrestrial reference frame, observing Earth rotation parameters (ERP) and the Earth's long-wavelength gravitational potential with a previously unprecedented accuracy. SLR confirmed the theory of the drift of tectonic plates and allowed defining the precise value of one of the fundamental values in physics and astronomy, i.e., the standard gravitational parameter of the Earth GM. The SLR technique remains constantly crucial in many fields of the space geodesy, even though it has been nowadays superseded in many fields by other space geodesy techniques. The densification of the reference frame and ERP are better established by the Global Navigation Satellite Systems (GNSS), and the Earth gravity field by the dedicated missions: CHAMP, GRACE, and GOCE. Nevertheless, the contribution of SLR to the definition of the origin of the reference frame (geocenter coordinates), the global scale, GM, and low degree spherical harmonics of the Earth's gravity field (especially the oblateness term) is essential due to the remarkable orbit accuracy of geodetic satellites and the precision of laser observations at a level of a few millimeters. Considering these aspects, SLR has an exceptional potential in establishing global networks and deriving geodetic parameters of the supreme quality [7]. The accuracy and precision of SLR measurements have greatly improved in recent years, allowing for more detailed studies and new applications. SLR is a valuable tool for studying the Earth's environment, geodesy, and fundamental physics, and is expected to remain an important technique for many years to come.

2.2 International Laser Ranging Service

The International Laser Ranging Service (ILRS) [8] was established in 1998 by the International Association of Geodesy (IAG). The primary goal of the ILRS was to develop a global network of SLR stations to support programs in geodesy, geophysics, fundamental constants and lunar research, and to provide the International Earth Rotation Service with data products that are essential to the maintenance and improvement in the International Terrestrial Reference Frame (ITRF).

Over the years, the ILRS has grown to become a global network of over 40 SLR stations, covering all continents except for Antarctica. The data produced by the network is used for a wide range of scientific and practical applications, including satellite orbit determination and validation, Earth rotation monitoring, and studies of the Earth's gravity field and its variations.
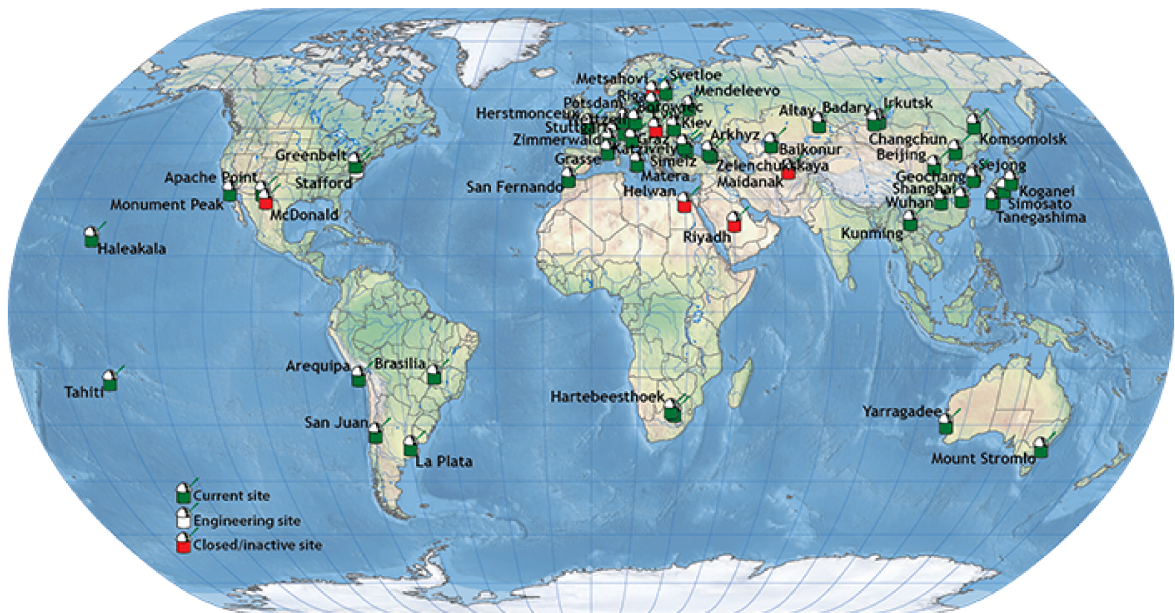

Figure 2.3: ILRS network stations.

In addition to its scientific and practical applications, the ILRS is also an important international collaboration that helps to promote cooperation and exchange of knowledge and expertise among the global geodetic community. The network is operated by a wide range of organizations, including national space agencies, universities, and research institutions, and the data produced by the network is freely available to researchers and other users around the world.

The ILRS stations track more than ninety satellites from low Earth orbit (LEO) to the geosynchronous orbit altitude as well as retroreflector arrays on the surface of the Moon. Applications have been expanded to include time transfer, asynchronous ranging for targets at extended ranges, free space quantum telecommunications, and

the tracking of space debris.[9]

2.3 Corner Cube Retroreflectors (CCR)

Corner Cube Retroreflectors (CCRs) are optical devices that consist of three mutually perpendicular reflective surfaces that intersect at a single point, forming a corner. These surfaces are designed to reflect light back to its source regardless of the angle of incidence. In general, CCRs can be classified as [10]:

- Hollow corner cubes

- Uncoated solid total internal reflection (TIR) corner cubes

- Back-coated solid corner cubes

Hollow CCRs are formed by three flat mirrors that enclose a hollow cavity. The mirrors are typically made of metal or dielectric coated glass. Hollow corner cubes have several advantages over solid glass corner cubes : they are lighter in weight, less expensive to manufacture, and have a narrow far field diffraction pattern. The main issues of hollow CCRs are thermal heating and gradient effects on joints. Currently hollow CCRs are not used in the visible, but recent developments [11] aim to use hollow CCRs for more precise Lunar Laser Ranging (LLR).
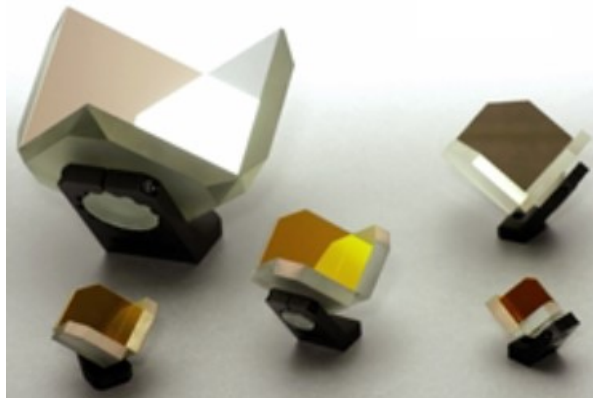

Figure 2.4: Hollow CCRs.

Uncoated solid CCRs consists in three reflective surfaces made of the same material, typically glass or quartz, not coated with any reflective material. One advantage of solid uncoated corner cubes is that they have a very wide bandwidth of reflection, meaning that they can reflect light across a broad spectrum of wavelengths. They have fewer thermal problems than hollow CCRs but they show reflection leaks when incidence angle is higher than 17°. Also, they are polarization sensitive, which means that return signal can be reduced by a factor of 4. Uncoated CCRs were widely used at the beginning of SLR history (LAGEOS, Apollo) but now are rarely used.
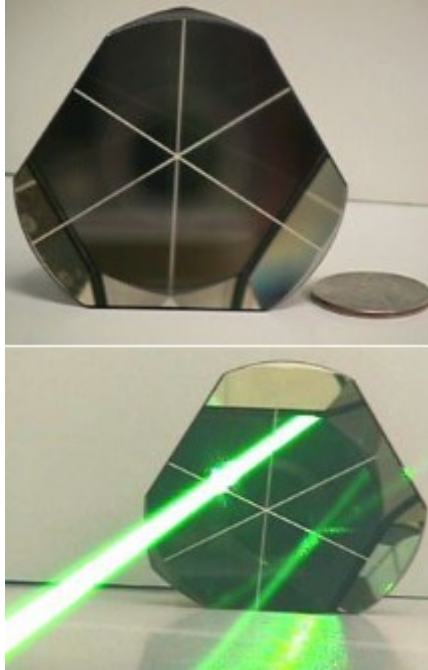
Figure 2.5: Solid CCRs.

Coated solid CCRs are solid CCRs with the addition of a metal coating (typically aluminum or silver) on the reflective surfaces. This can limit the reflection bandwidth for specific applications, but its main advantage is removing the polarization effects typical of uncoated CCRs. These advantages come with a cost, as metal coatings absorb sunlight and create thermal gradients. Coated CCRs are now the most commonly used for space applications and can be found on most satellites with SLR capabilities.

2.4 Millimeter accuracy

The history of SLR accuracy is tied to the ground equipment's technology improvements. The first SLR returns were recorded on October 31, 1964 at Goddard Space Flight Center (GSFC). The ground equipment at the time consisted in a rotating mirror Q-switched ruby laser at a 694 nm wavelenght, 0.8 J energy and a 1 Hz repetition rate. The telescope's pointing control system consisted of two joysticks, one for azimuth and the other for elevation, controlled manually by two operators. Ranging accuracy at the time was around 3 m. In 1969, when Don Premo of GSFC introduced computer control of the tracking mount, daytime SLR became possible and ranging accuracy improved from 3 m to 1 m. At the beginning of the 70s, the first generation trailer based Mobile Laser systems were developed by NASA/GSFC (MOBLAS 1 through 3) and cooperated with two French stations in early science experiments. This marked the transition from ruby to Nd:YAG lasers which are still used nowadays [12].
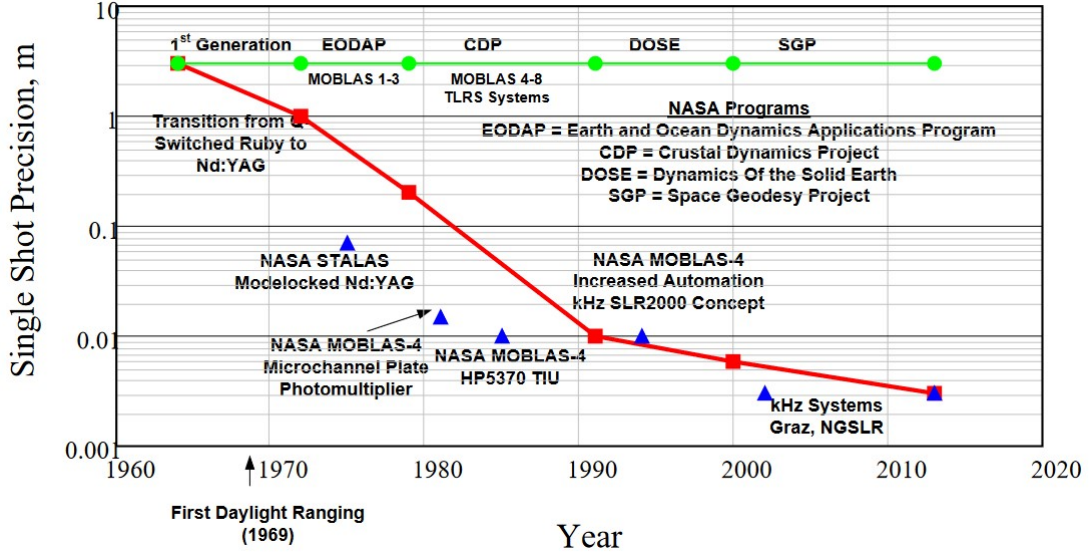
Figure 2.6: Nominal best SLR accuracies vs time (red).

Two colors SLR offers the potential of an order of magnitude improvement in ranging absolute accuracy, but the technique requires high precision differential time measurements. This can be achieved with short pulses, high signal levels and temporal averaging [13].

To maximize the individual range measurement precision is crucial to minimize the variance in the pulse Time Of Flight (TOF) measurement which is the sum of the variances introduced by the individual subsystems, including the space target, and given by

$$\sigma_{Total}^2 = \sigma_{Laser}^2 + \sigma_{Detector}^2 + \sigma_{Timer}^2 + \sigma_{Target}^2 \tag{2.1}$$

Analysts determining the satellite orbits always average over N individual "Full Rate Measurements" to form "Normal Points" for a segment of the orbital arc which have an improved range precision given by

$$\Delta R_{NP} = \frac{\sigma_{Total}}{\sqrt{N}} \tag{2.2}$$

Thus, as the laser pulse frequency increases, the faster the desired normal point range precision can be achieved. In addition, the resulting normal point can represent a shorter orbital arc length and therefore a higher spatial resolution orbit.

The next big advance in SLR technology was in 1994 as SLR2000, an autonomous and eyesafe station with an expected single shot range precision of about one centimeter and a normal point precision better than 3 mm was proposed [14]. Single photon ranging using eyesafe laser beams eliminated need for aircraft safety radars and observers. Also, semi-autonomous operations (1 operator per station per shift vs 3 to 4 for MOBLAS) reduced notably the financial burden on the SLR network, as the growing number of satellites needed more and more time allocation and operators. The system was funded in 1997 and the 2 kHz ranging improved normal

point resolution by roughly an order of magnitude. From there, improvements in detector and time measuring technologies brought maximum accuracy to the actual level of roughly 1-2.5 mm achieved at stations like the one in Graz.

Figure 2.7: Graz SLR station during night operations.

2.5   Attitude determination

The increasing accuracy and resolution of SLR systems enabled the possibility of precise attitude determination from the ground. There are two main methods to determine the attitude using SLR data: the first one resolves the attitude from the motion of the CCR around the center of mass while the other uses multiple CCRs and compares their measured ranges to get incident angles.

The first method was first used in 2007 to determine the spin parameter of the Ajisai satellite and again in 2014 to determine attitude and spin period of Envisat. In the first case, due to the axial rotation of Ajisai and the well-separated reflector panels, arranged in rings, the distance from the observer to each panel varies periodically. The periods are given by the spin rate of the satellite and the number of panels of the involved ring. The amplitudes depend on the dimension of the sphere, the distance between the panels, and the incidence angle of the laser beam. A spectral analysis was performed on SLR data, and it was shown that each calculated frequency corresponds to a specific number of CCR panels. The ratio between the frequency and the number of panels of the corresponding ring gives the exact spin rate of Ajisai [15].
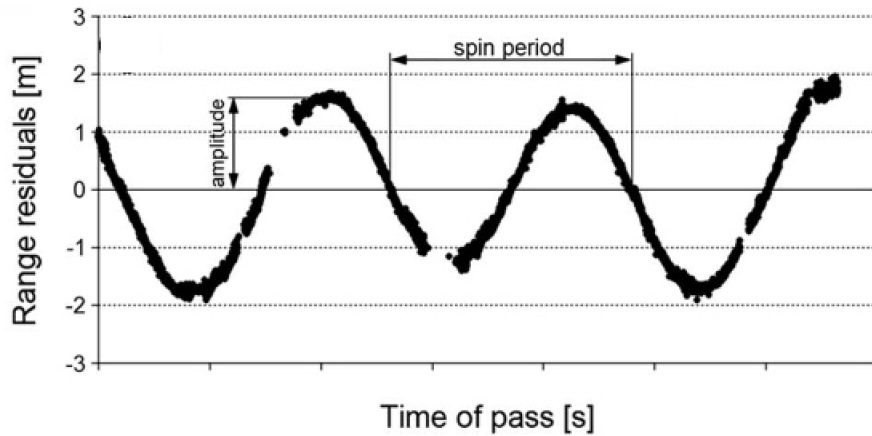
Figure 2.8: Envisat spin period shown from range residuals.

The same method was used for Envisat, as the rotation of the retroreflector panel about the spin axis causes oscillations of the range measurements in the meter scale. This effect is clearly visible in the distribution of the range residuals calculated as observed minus predicted range. The range residuals oscillate due to an offset between the spin axis and the retroreflector panel, and the oscillation period can be determined by frequency analysis of the given data set [16].
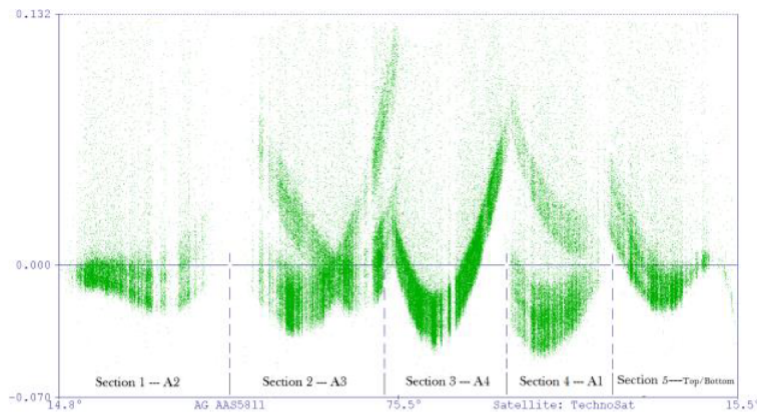

Figure 2.9: Five faces of TechnoSat tracked in Graz on 2018/03/22. Individual CCR traces are visible.

The second method was demonstrated multiple times, for example in 2013 and 2019 as experiments at ground level and in 2018 on a flying satellite. Having multiple CCRs placed at a certain distance and measuring the range difference allows to compute the laser incident angle. This requires the resolution and accuracy of a kHz SLR system, as range measurement errors translate in angle errors and also is crucial to distinguish CCR traces. On the ground this method was tested at Graz using a simple bar with 2 CCR mounted [17] and also a spare Galileo CCR array [18], in both cases being able to compute incident angles with great accuracy. The TechnoSat mission, currently operational and tracked by the ILRS, has 14 Commercial Off The

17

Shelf (COTS) CCRs on board, placed on every face of the satellite. Individual CCR traces could be distinguished using the SLR system in Graz proving that 10 mm commercial CCRs can be used successfully for precise orbit determination, but also for attitude and attitude motion determination independently of the operational status of the satellite [19].

AlbaSat CCR payload development

This chapter discusses the development process of the CCR payload onboard the AlbaSat mission. In the first section, from mission objectives and constraints a series of technical requirements was obtained. The second section explains the design philosophy chosen, with major milestones and expected hardware models. Then, a series of analyses conducted to assess CCR performance is reported. For these analyses CCRs of different commercially available diameters are considered and numerical simulations have been performed representing various operative situations. From the results of these simulations, a trade-off analysis was conducted to choose the optimal CCR diameter, quantity and their configuration on the spacecraft. Figure 3.1 shows how the reference frame used on the spacecraft. From now on axes will be referenced using this frame.
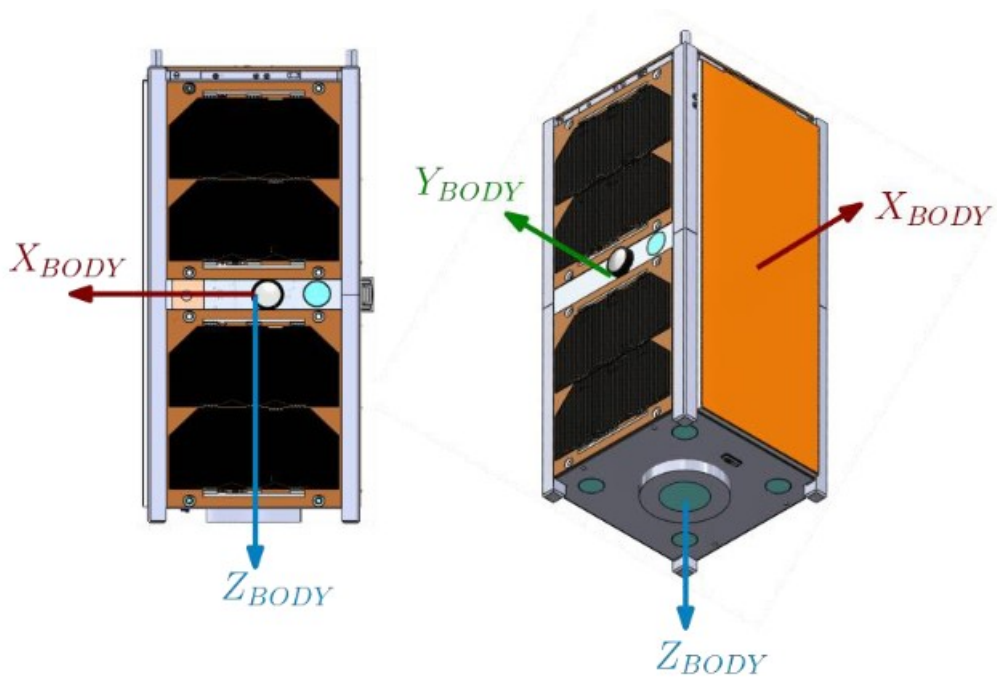

Figure 3.1: Axes references.

3.1 Technical requirements

The requirements definition process is critical to determine the main features of the design and to understand the expected performance. Following the ECSS standard [20], technical requirements are split in :

- **Mission requirements (MIS)**: represent the main purpose of the payload and they come directly from the mission objectives.

- **Functional requirements (FKT)**: represent how the payload is going to accomplish the mission objectives.

- **Configuration requirements (CON)**: declare if there are some specific needs regarding the configuration of the payload.

- **Interface requirements (INT)**: declare needed compatibilities with other subsystems and/or equipment.

- **Performance requirements (PRF)**: declare the required performance level of what is being done.

Given this classification, it's easier to translate technical needs in a functional design. Requirements for this payload are shown in Table 3.1.

The mission objective is to perform orbit and attitude determination through laser ranging, that translates directly in mission requirement SYS-MIS-300. The consequence of this objective is the first functional requirement SAT-FKT-301, as the reflection of a laser beam is needed to perform laser ranging measurements. This is a requirement at a system level, and determined the choice of putting CCRs on the spacecraft.

Laser ranging measurements are considered to be done by the ILRS network, and as the vast majority of ILRS stations use 532 nm lasers [6], the payload has to be designed to reflect this wavelenght. From this need are derived interface and performance requirements PL-CCR-INT-305 and PL-CCR-PRF-306. These requirements determine the choice of a CCR coating to reflect the 532 nm wavelenght and a diameter which guarantee signal detection and is within dimensional constraints.

The payload has been designed to allow laser ranging measurements after spacecraft end of life and/or loss of attitude control, so configuration and functional requirements PL-CCR-CON-303 and PL-CCR-FKT-307 were included. This led to avoiding mechanisms in the design and considering mounting CCRs on multiple faces of the spacecraft.

Orbital determination accuracy is dependent on ground station performance only [13], so no requirements are needed for this mission objective. Attitude determination requires multiple CCRs and their configuration has an effect on obtainable accuracy [17] [18]. So performance requirement PL-CCR-PRF-308 was included.

Constraints on other spacecraft faces (e.g. solar panels) led to the choice of doing attitude determination with CCRs on the $+Z$ face only. CCRs on other faces are intended for orbital determination only.

Table 3.1: Technical requirements for the CCR payload.

Identifier	Text
SYS-MIS-300	The mission shall measure position and the attitude of the satellite through laser ranging.
SAT-FKT-301	The CubeSat shall return a laser beam.
PL-CCR-CON-303	The CCR payload shall be passive.
PL-CCR-INT-305	The CCRs shall be compatible with the use of the ILRS infrastructure.
PL-CCR-PRF-306	The CCR shall work with a wavelength of 532 nm.
PL-CCR-FKT-307	The payload shall grant the possibility to compute orbit determination in case of loss of attitude control.
PL-CCR-PRF-308	The CCRs on the +Z face shall allow the attitude determination with accuracy of minimum 30 deg.

3.2 Design philosophy

CCRs are commercial components with extensive flight heritage, relatively cheap and readily available from various suppliers. The main topic of this chapter is the choice of a number of commercial CCRs and their configuration on the spacecraft. To mount the CCRs on the spacecraft, a custom holding structure has to be designed and tested.

The mission model philosophy is different between the subsystems and the CCR, IS, MVS and QPL payloads. The subsystems follows a BBM (BreadBoarding Model) + EM (Engineering Model) + PFM (ProtoFlight Model) model philosophy while the IS, MVS and QPL payloads follow a BBM + DM (Development Model) + EQM (Engineering-Qualification Model) + FM (Flight Model) approach. This has been chosen since, while COTS components are used for the subsystems, these payloads are developed in house. For what concerns the CCR payload, it follows a DM+EQM+PFM approach, this is because of the flight heritage of CCRs as components.

After the consolidation of the design at system level, the selection of the COTS CCR is reviewed and confirmed. A DM consisting of a 3D printed structure and a purchased CCR will be built to check assembly and dimensions. The EQM is then designed and the components are procured. The CCRs are purchased by specialized industries while the structure is produced in house. A qualification and verification

test campaign is conducted on the EQM and optical tests are performed.

The results are used to consolidate the design of the PFM. Once that the critical design is reached, the CCRs are procured and the structure is produced. After a validation and verification test campaign they are integrated in the PFM of the system. Environmental tests are performed at system level.

The results of the analyses done in this work led to the production of the DM, currently built and under verifications. The EQM production deadline is currently set for December 2023, and will undergo a vibration and thermo-vacuum test campaign.
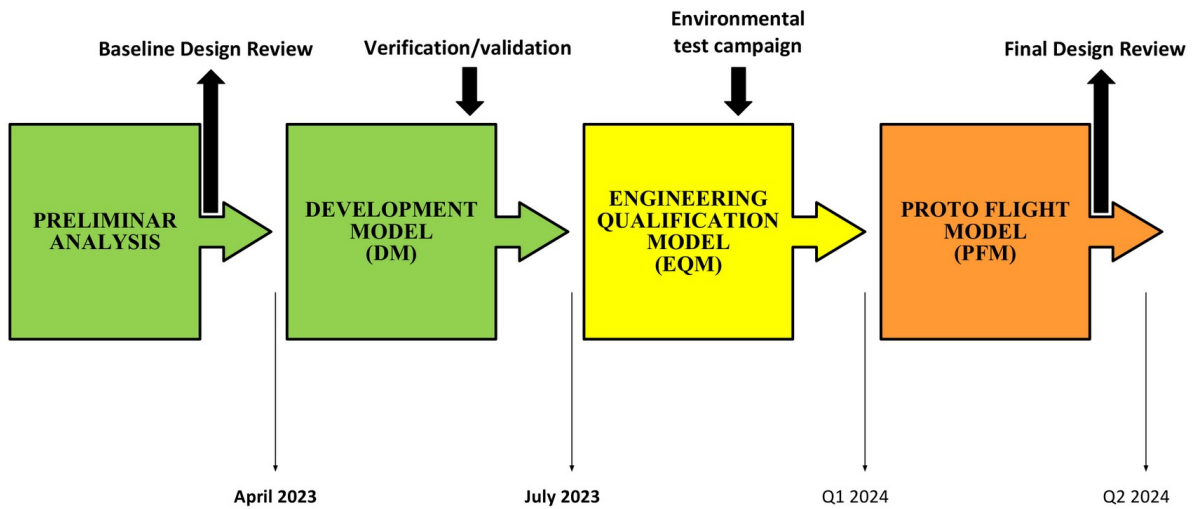

Figure 3.2: Design process and expected timeline.

3.3 Performance analysis

3.3.1 Link budget

In order to select a CCR type and diameter compliant with the functional and performance requirements SAT-FKT-301, PL-CCR-INT-305, PL-CCR-PRF-306 a link budget analysis was set up. Laser link equation was used to evaluate the mean number of photoelectrons received for every transmitted laser pulse. The main objective is to determine detection probability in multiple operative conditions. The mathematical model of the link budget was first proposed by Degnan [13].

Assumptions and limitations

Laser link equation The laser link equation provides an estimate of photon return based on laser energy, range, array cross section, optics efficiency and weather:

$$N_{pe} = \eta_q \left(\frac{E_T}{hv} \right) \eta_T G_T \sigma_{eff} \left(\frac{1}{4\pi R^2} \right)^2 A_R \eta_R T_A^2 T_C^2 \tag{3.1}$$

where η_q is the quantum efficiency of the receiver, E_T is the laser pulse energy in mJ, hv is the photon energy ($3.73 \cdot 10^{-19}$ J at 532 nm) η_T is the efficiency of the transmitting optics, G_T is the laser beam gain, σ_{eff} is the CCR optical cross section (OCS), R is the slant range to the target, A_R is the telescope aperture, η_R is the efficiency of the receiving optics, T_A is the one way atmospheric transmission and T_C is the one way transmissivity of cirrus clouds, if present. The result N_{pe} is the mean number of photoelectrons seen at the receiver.

OCS The peak optical cross section of a corner cube retroreflector is:

$$\sigma_S = \frac{\rho(\pi^3 D^4)}{(4\lambda)^2} \tag{3.2}$$

where ρ is the reflectivity (0.78 for Al coated CCRs), D is the CCR diameter and λ is the laser wavelength. OCS is affected by incidence angle θ_{inc}:

$$\sigma_{eff}(\theta_{inc}) = \eta^2(\theta_{inc})\sigma_S \tag{3.3}$$

Where $\eta(\theta_{inc})$ is the reduction factor:

$$\eta(\theta_{inc}) = \frac{2}{\pi}(sin^{-1}\mu - \sqrt{2}tan(\theta_{ref}))cos(\theta_{inc}) \tag{3.4}$$

θ_{ref} is the internal refracted angle:

$$\theta_{ref} = sin^{-1}\left(\frac{sin(\theta_{inc})}{n} \right) \tag{3.5}$$

n is the cube index of refraction (1.455 for fused silica). The quantity μ is equal to:

$$\mu = \sqrt{(1 - tan^2\theta_{ref})} \tag{3.6}$$

Transmitter gain (G_T) The transmitter gain for a gaussian beam is:

$$G_T = \frac{8}{(\theta_t^2)} exp \left[-2 \left(\frac{\theta_p}{\theta_t} \right)^2 \right] \tag{3.7}$$

where θ_t is the far field divergence half angle of the beam and θ_p is the beam pointing error.

Slant range (R) The slant range is given by the expression:

$$R = -(R_E + h_{GS})cos(\theta_{zen}) + \sqrt{(R_E + h_{GS})^2 cos^2(\theta_{zen}) + 2R_E(h_S - h_{GS}) + h_S^2 - h_{GS}^2} \tag{3.8}$$

where R_E is the Earth radius, h_{GS} is the station altitude, h_S is the satellite altitude and θ_{zen} is the zenith angle. For these simulations, a MATLAB function from the Aerospace Toolbox is used to compute slant range. Slant range is the most relevant parameter as number of returning photons decrease with the fourth power of range, so spacecraft altitude is crucial.

Atmospheric transmission (T_A) Atmospheric transmission is a function of the zenith angle:

$$T_A(\lambda, V, 0) = exp \left[-\sigma(\lambda, V, 0) h_{SH} sec(\theta_{zen}) exp \left(-\frac{h_{GS}}{h_{SH}} \right) \right] \tag{3.9}$$

Where $\sigma(\lambda, V, 0)$ is the attenuation coefficient at wavelength λ and with sea level visibility V, h_{GS} is the ground station altitude and h_{SH} is the scale height, equal to 1.2 km.

Cirrus transmittance (T_C) Cirrus transmittance is function of zenith angle and mean cirrus cloud thickness:

$$T_C = exp \left[-0.14(t \cdot sec(\theta_{zen}))^2 \right] \tag{3.10}$$

Where $t = 1.341$ km is the mean cirrus cloud thickness.

Photoelectron generated from background noise To evaluate signal detection capabilities background noise must be determined:

$$N_B = \frac{\eta_q}{h\upsilon} N_\lambda \lambda_{BP} \Omega_R A_R \eta_R \tau_{RG} \tag{3.11}$$

Where N_λ is the background spectral radiance (night sky provide a noise background of $3 \cdot 10^{-6} \frac{W}{ster} m^2$, while sunlit clouds provide a noise background of $1.4 \cdot 10^8 \frac{W}{ster} m^2$), Ω_R is the detector FOV solid angle in steradians, λ_{BP} is the width of the bandpass filter and τ_{RG} is the temporal width of the range gate.

$$\Omega_R = \left(\frac{\theta_{FOV}}{2} \right)^2 \tag{3.12}$$

Where θ_{FOV} is the detector FOV half angle in radians.

Probability of signal detection Since the photon detection follows the Poisson probability distribution, the probability per laser pulse of detecting m number of photons, where N is the average number of photoelectrons:

$$P(m, N) = \frac{N^m}{m!} e^{(-N)} \tag{3.13}$$

Then the probability of detecting one photon from the background noise which is the false alarm probability:

$$P_{FA} = 1 - e^{(-N_B)} \tag{3.14}$$

The photon detection probability, which is the probability of detecting one photon from the background noise and actual signals, is:

$$P_{PD} = 1 - e^{(-N)} \tag{3.15}$$

Where $N = N_{PE} + N_B$ is the total photoelectrons number. Finally, the signal detection probability, probability of detecting a signal from the background noise, is:

$$P_{SD} = (1 - P_{FA}) P_{PD} \tag{3.16}$$

Limitations The descripted model for simulating CCR photon return does not consider velocity aberration. As the spacecraft is going to be in LEO, the higher orbital velocity might reduce photon return. Effects of velocity aberration are going to be investigated in a further analysis. Also, attitude errors are not being considered.

Analysis description

For this analysis, parameters from all stations of the ILRS network capable of LEO laser ranging were collected [6]. In Table 3.2 is shown an example of parameters from the Matera station. For all stations parameters see Appendix A.

Table 3.2: Parameters for Matera station.

Station Parameter	Value
E_T	100 mJ
f	10 Hz
Pulse width	50 ps
η_q	0.4
η_T	0.75
η_R	0.87
A_R	1.5 m
θ_D	$9.71 \cdot 10^{-6}$ rad
θ_P	$4.85 \cdot 10^{-6}$ rad
w_0	0.01 m
λ_{BP}	0.3 nm
θ_{FOV}	$2.91 \cdot 10^{-4}$ rad
τ_{RG}	20 ns
h_{GS}	536.9 m

The analysis are performed through a MATLAB script which reads stations parameters from an Excel file, computes slant range, atmospheric transmission, cirrus transmission, OCS, number of return photoelectrons, and then calculates the probability of detection for every zenith angle θ_{zen} from 0 deg (directly overhead) to 70 deg (tracking limit for most stations), with 1 deg steps.
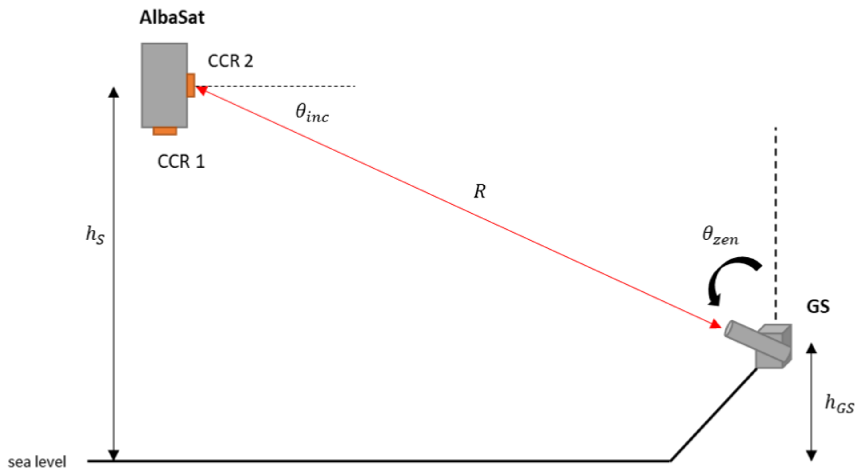

Figure 3.3: Link budget simulation configuration.

The simulated scenario is shown in Figure 3.3. For the analyses aluminium coated CCR are considered. As for the dimensions, only the commercially available

diameters are taken in consideration. In particular, the CCR diameters considered are 7.16 mm, 10 mm, 12.7 mm and 25.4 mm. The wavelenght of the laser beam has been set to 532 nm, as it is the most common among ILRS stations. Al coated CCRs were chosen to be compliant with requirements PL-CCR-INT-305 and PL-CCR-PRF-306. Three mission candidate orbits were considered, with altitudes of 470 km, 500 km and 530 km. Attitude is nadir-pointing, and pointing errors are not considered in this analysis. FOV half-angle of CCRs is assumed to be 30 deg [13]. To ensure signal return on most situations, 2 CCR are simulated, one on the nadir face of the spacecraft reflecting the beam for zenith angles from 0 deg to 30 deg and another on the side face reflecting the beam for zenith angles from 60 deg to 70 deg. To build the operational envelope of every CCR diameter a best, worst and average scenarios were considered, combining atmospherical conditions and orbital altitudes. For the best case scenario the spacecraft is assumed to be at 470 km altitude, on an extremely clear day with 60 km visibility and no cirrus. For the average case scenario the spacecraft is assumed at 500 km altitude, on a clear day with 15 km visibility and cirrus presence. For the worst case scenario the spacecraft is assumed at 530 km altitude, on a light hazed day with 8 km visibility and cirrus presence. A summary of simulation parameters for every case is shown in Table 3.3.

Table 3.3: Simulation parameters in different scenarios.

Parameter	Best Case	Average Case	Worst Case
h_S	470 km	500 km	530 km
λ	532 nm		
θ_{ZEN}	0-30 deg / 60-70 deg		
ρ	0.78 (Al coating)		
n	1.455 (for fused silica)		
t	0 (no cirrus)	1.348 km	1.348 km
$\sigma(\lambda, V_0)$	0.18 (60 km visibility)	0.25 (15 km visibility)	0.46 (8 km visibility)
θ_{CCR}	30 deg		
N_λ	$3 \cdot 10^{-6}$ $W/ster \cdot m^2$ for night sky $1.48 \cdot 10^8$ $W/ster \cdot m^2$ for daytime		

Analysis results

As the detection probability is expressed per laser pulse, a 50% or higher detection probability for more than 2 angle steps is considered to guarantee detection of a given CCR. Table 3.4, Table 3.5 and Table 3.6 show best, average and worst case percentages of ILRS stations detecting the illuminated CCR in a zenith angle range, for night operations. Table 3.7, Table 3.8 and Table 3.9 show best, average and worst case percentages for day operations. Night SLR operations are feasible with all ILRS stations and with all CCR diameters for lower zenith angles when spacecraft is directly overhead. As the angle increases, contact losses with ground stations occurs faster with lower diameter CCR.

Table 3.4: ILRS stations with detection probability >50% - NIGHT BEST

CCR reflecting	θ_{zen}	7.16 mm	10 mm	12.7 mm	25.4 mm
CCR 1 (nadir)	0° - 30°	100%	100%	100%	100%
CCR 2 (lateral)	60° - 70°	89%	100%	100%	100%

Table 3.5: ILRS stations with detection probability >50% - NIGHT AVERAGE

CCR reflecting	θ_{zen}	7.16 mm	10 mm	12.7 mm	25.4 mm
CCR 1 (nadir)	0° - 30°	100%	100%	100%	100%
CCR 2 (lateral)	60° - 70°	58%	64%	87%	98%

Table 3.6: ILRS stations with detection probability >50% - NIGHT WORST

CCR reflecting	θ_{zen}	7.16 mm	10 mm	12.7 mm	25.4 mm
CCR 1 (nadir)	0° - 30°	100%	100%	100%	100%
CCR 2 (lateral)	60° - 70°	53%	64%	74%	92%

Fewer ILRS stations are capable of daytime laser ranging to this payload. For these stations, performance degradation is similar to night operations, but with overall lower detection probabilities. Note that possible further sunlight attenuation filters are not considered in this simulation, so there could be more stations capable of daytime laser ranging to this payload.

Table 3.7: ILRS stations with detection probability >50% - DAY BEST

CCR reflecting	θ_{zen}	7.16 mm	10 mm	12.7 mm	25.4 mm
CCR 1 (nadir)	0° - 30°	43%	43%	43%	43%
CCR 2 (lateral)	60° - 70°	38%	43%	43%	43%

Table 3.8: ILRS stations with detection probability >50% - DAY AVERAGE

CCR reflecting	θ_{zen}	7.16 mm	10 mm	12.7 mm	25.4 mm
CCR 1 (nadir)	0° - 30°	43%	43%	43%	43%
CCR 2 (lateral)	60° - 70°	20%	28%	35%	43%

Table 3.9: ILRS stations with detection probability >50% - DAY WORST

CCR reflecting	θ_{zen}	7.16 mm	10 mm	12.7 mm	25.4 mm
CCR 1 (nadir)	0° - 30°	43%	43%	43%	43%
CCR 2 (lateral)	60° - 70°	17%	20%	28%	41%

Figures 3.4 and 3.5 show a detail of performance variation with diameter and conditions at BORL station for night operations.
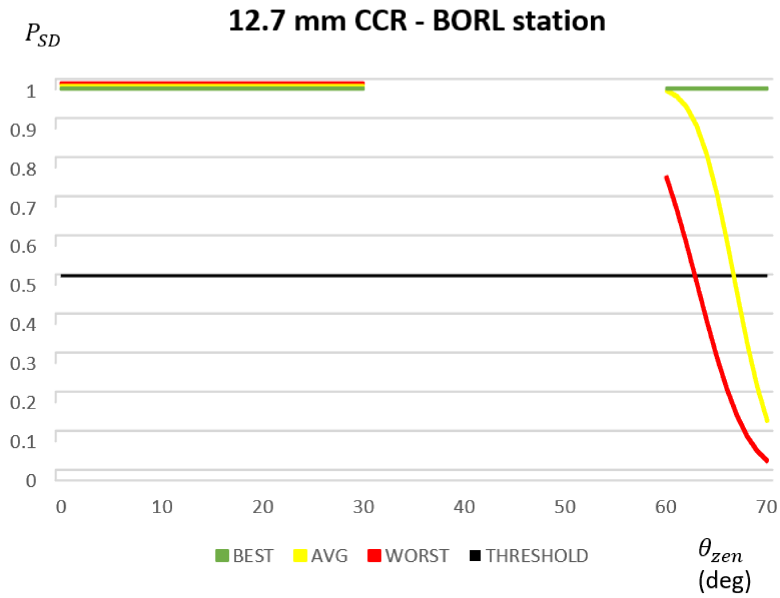

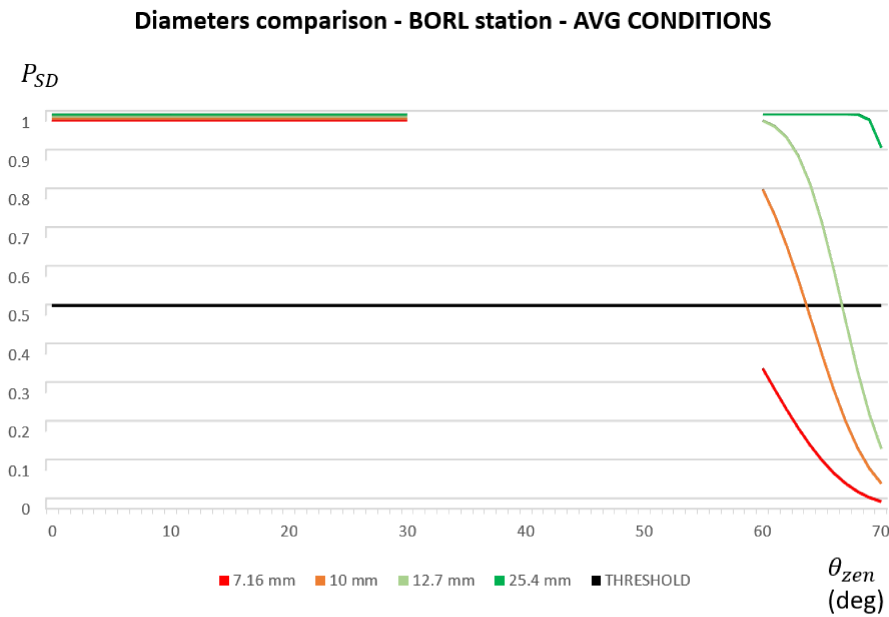Figure 3.4: Best, average and worst performance of a 12.7 mm CCR for BORL station at night.

Figure 3.5: Performance of various CCR diameters for BORL station at night with average conditions.

3.3.2 Laser power budget

In order to evaluate average laser power return seen at the detector and SNR with all ILRS stations, a power budget analysis was set up. This was done calculating the channel losses through the clipping of a gaussian beam, as shown in Tomaello et al. [21].

Assumptions and limitations

Laser average power   For a pulsed laser beam with pulse energy E_T and pulse frequency f, the average power is:

$$P_{AVG} = E_T f \tag{3.17}$$

Pulse energy and frequency are parameters publicly available for every ILRS station [6].

Propagation of a gaussian beam   The width of a laser beam spot at a given distance R and for a given starting beam width w_0 is:

$$w(R) = w_0 \sqrt{1 + \left(\frac{\lambda R}{(\pi w_0^2)}\right)^2} \tag{3.18}$$

Where R is the slant range from station to spacecraft, calculated in the same way as for the link budget analysis.

Power transmittance   Channel losses at the receiving end are:

$$\eta = \eta_0 \left(1 - exp\left(-\frac{2D_{REC}^2}{w(R)^2}\right)\right) \tag{3.19}$$

Where D_{REC} is the diameter of the receiver and the factor η_0 is function of zenith angle as:

$$\eta_0 = \eta_P \eta_T \eta_R 10^{\left(-\frac{4.34\tau sec(\theta_{zen})}{10}\right)} \tag{3.20}$$

Where η_P are pointing losses (≈ 0.2), η_T is transmitter optics efficency, η_R is receiver optics efficiency, τ is the depth of path at the zenith (≈ 0.8) and θ_{zen} is the zenith angle.

Power from signal   Average signal return power at the detector is:

$$P_{RET} = \eta_{UP}\eta_{DOWN}P_{AVG} \tag{3.21}$$

Where η_{UP} and η_{DOWN} are channel losses for uplink and downlink respectively.

Power from noise Power coming in the detector from background noise is:

$$P_B = N_\lambda \lambda_{BP} \Omega_R A_R \eta_R \tag{3.22}$$

Where N_λ is the background spectral radiance (sunlit clouds provide a worst-case noise background of $1.4 \cdot 10^8 \frac{W}{ster} m^2$), Ω_R is the detector FOV solid angle in steradians and λ_{BP} is the width of the bandpass filter.

SNR Signal to Noise ratio (in dB) is:

$$SNR = 10 log \left(\frac{P_{RET}}{P_B} \right) \tag{3.23}$$

Limitations The descripted model for simulating power return does not consider incidence angle of the beam on the CCR surface. For this analysis the spacecraft is assumed to be pointing a CCR to the ground station, so the beam has normal incidence. Also, velocity aberration is not considered. Further analysis is required as these factors may be not negligible.

Analysis description

In this scenario the spacecraft is pointing the +Z face towards the ground station for the whole duration. Three mission candidate orbits were considered, with altitudes of 470 km, 500 km and 530 km.
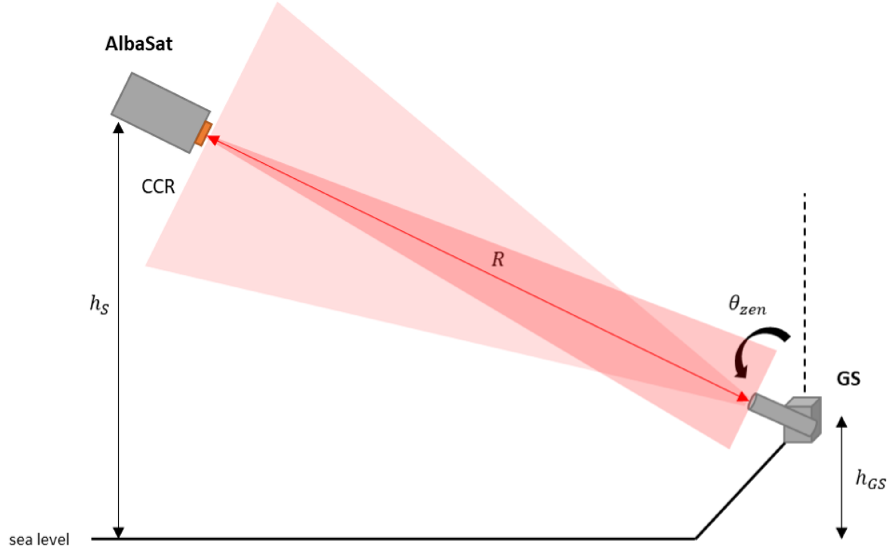

Figure 3.6: Laser power budget configuration.

Operation is split in uplink and downlink. For each part, a different set of parameters is used, these are shown in Table 3.10.

Table 3.10: Optical parameters for uplink and downlink.

	Uplink	**Downlink**
w_0 **starting beam diameter**	Beam width at telescope exit (from ILRS data)	CCR diameter
D_{REC} **receiving end diameter**	CCR diameter	Receiving telescope aperture (from ILRS data)

A MATLAB script reads ILRS stations parameters from an Excel file (see Appendix A). It then iterates on zenith angle (0° to 70°) and for every step compute slant range R, beam propagation $w(R)$ and channel losses η for uplink and downlink, using parameters shown in the table for each case. The script output is a table with return power in nW and SNR for every zenith angle and every ILRS station. In Table 3.11 is shown a summary of main simulation parameters.

Table 3.11: Power budget simulation parameters.

Parameter	Value	Description
λ	532 nm	Laser wavelength
h_S	470, 500, 530 km	Satellite altitude
θ_{zen}	0° - 70°	Zenith angle
N_λ	1.4×10^8 W/(ster m^2)	Background spectral radiance (sunlit clouds – worst case)
η_P	0.2	Pointing losses
τ	0.8	Depth path at zenith

Analysis results

Figures show SNR for EU based ILRS stations for each CCR diameter and each altitude. The minimum acceptable SNR is set to 2 (3 dB), shown in dotted red in the graphs. BORL station is not capable of daytime laser ranging to LEO satellites. Other stations show increasing performance with increasing CCR diameter. The minimum diameter for having acceptable SNR with all EU stations (except for BORL) is 12.7 mm. Performance is consistent with the link budget analysis for all ILRS stations.

Figure 3.7: SNR for EU stations for 7.16 mm diameter CCR - 470 km altitude.

Figure 3.8: SNR for EU stations for 7.16 mm diameter CCR - 500 km altitude.

Figure 3.9: SNR for EU stations for 7.16 mm diameter CCR - 530 km altitude.
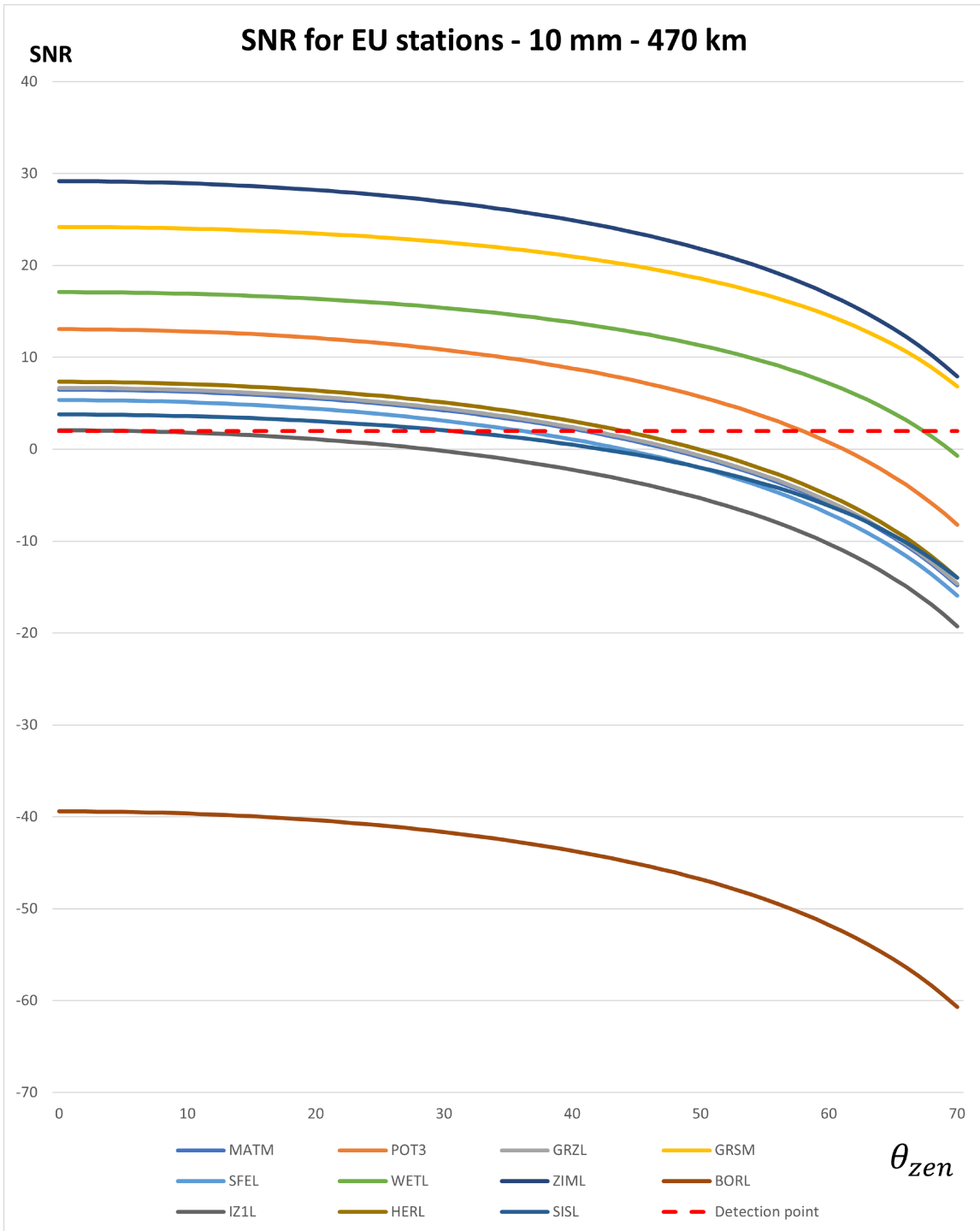
Figure 3.10: SNR for EU stations for 10 mm diameter CCR - 470 km altitude.
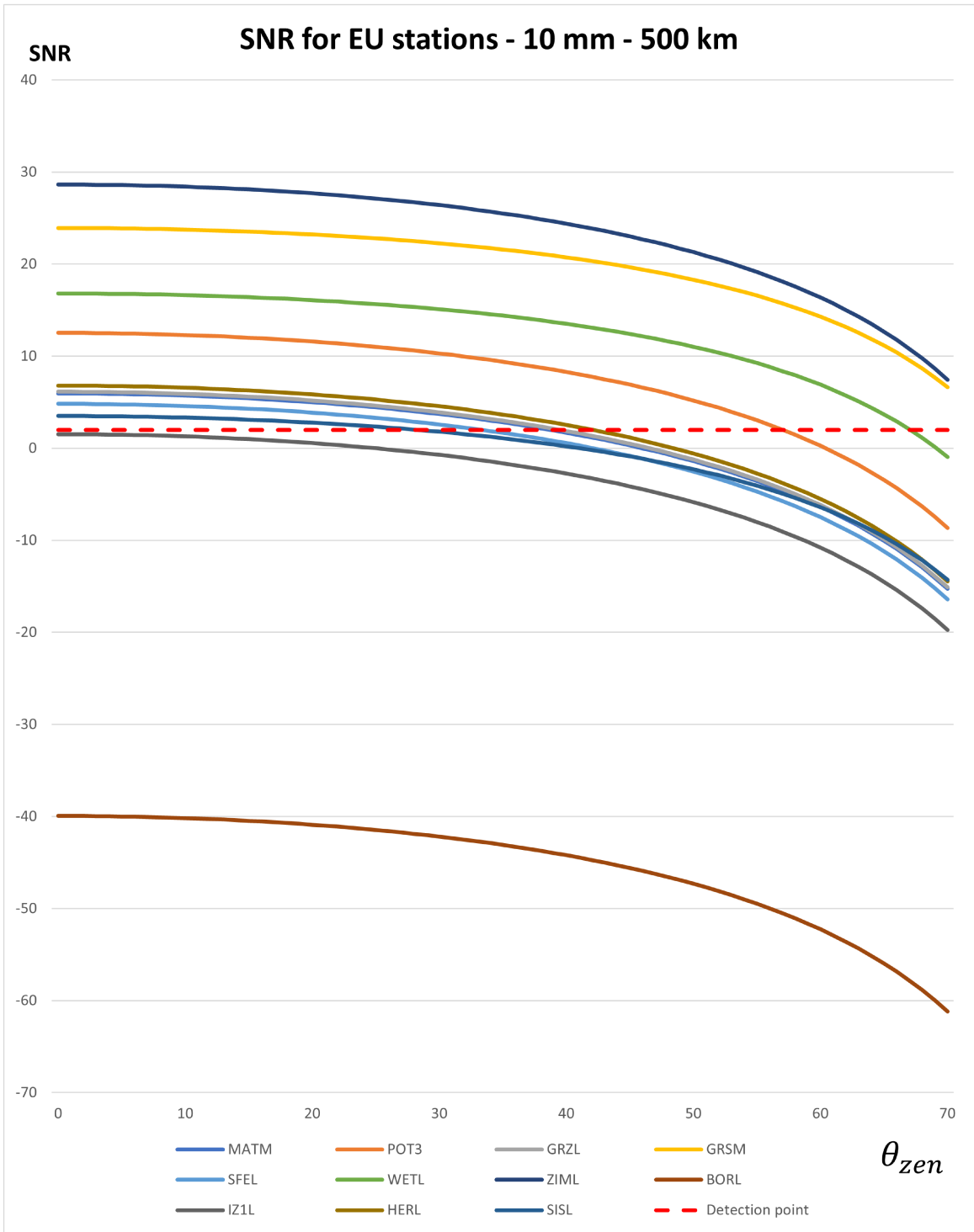
Figure 3.11: SNR for EU stations for 10 mm diameter CCR - 500 km altitude.

Figure 3.12: SNR for EU stations for 10 mm diameter CCR - 530 km altitude.

Figure 3.13: SNR for EU stations for 12.7 mm diameter CCR - 470 km altitude.

Figure 3.14: SNR for EU stations for 12.7 mm diameter CCR - 500 km altitude.

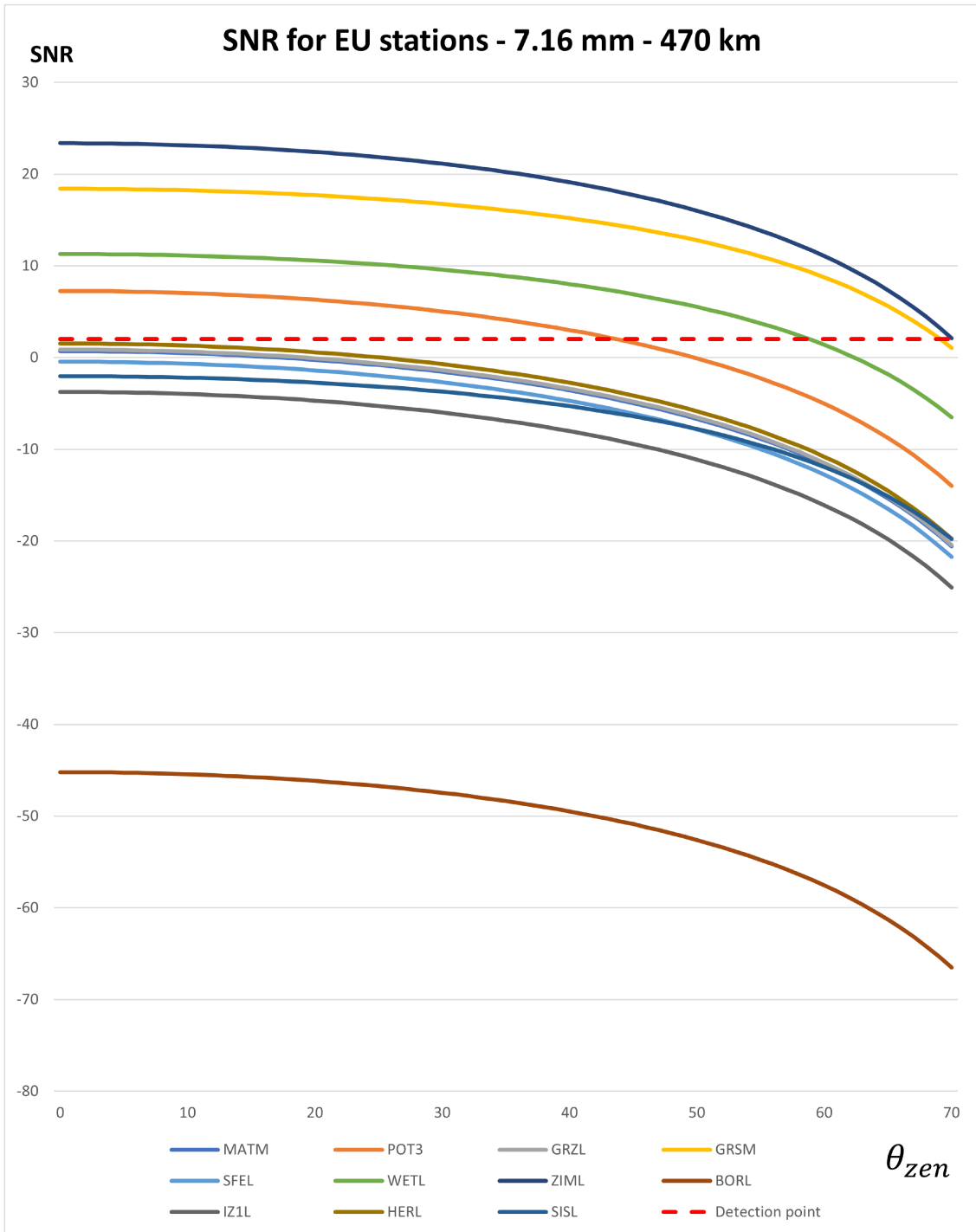Figure 3.15: SNR for EU stations for 12.7 mm diameter CCR - 530 km altitude.
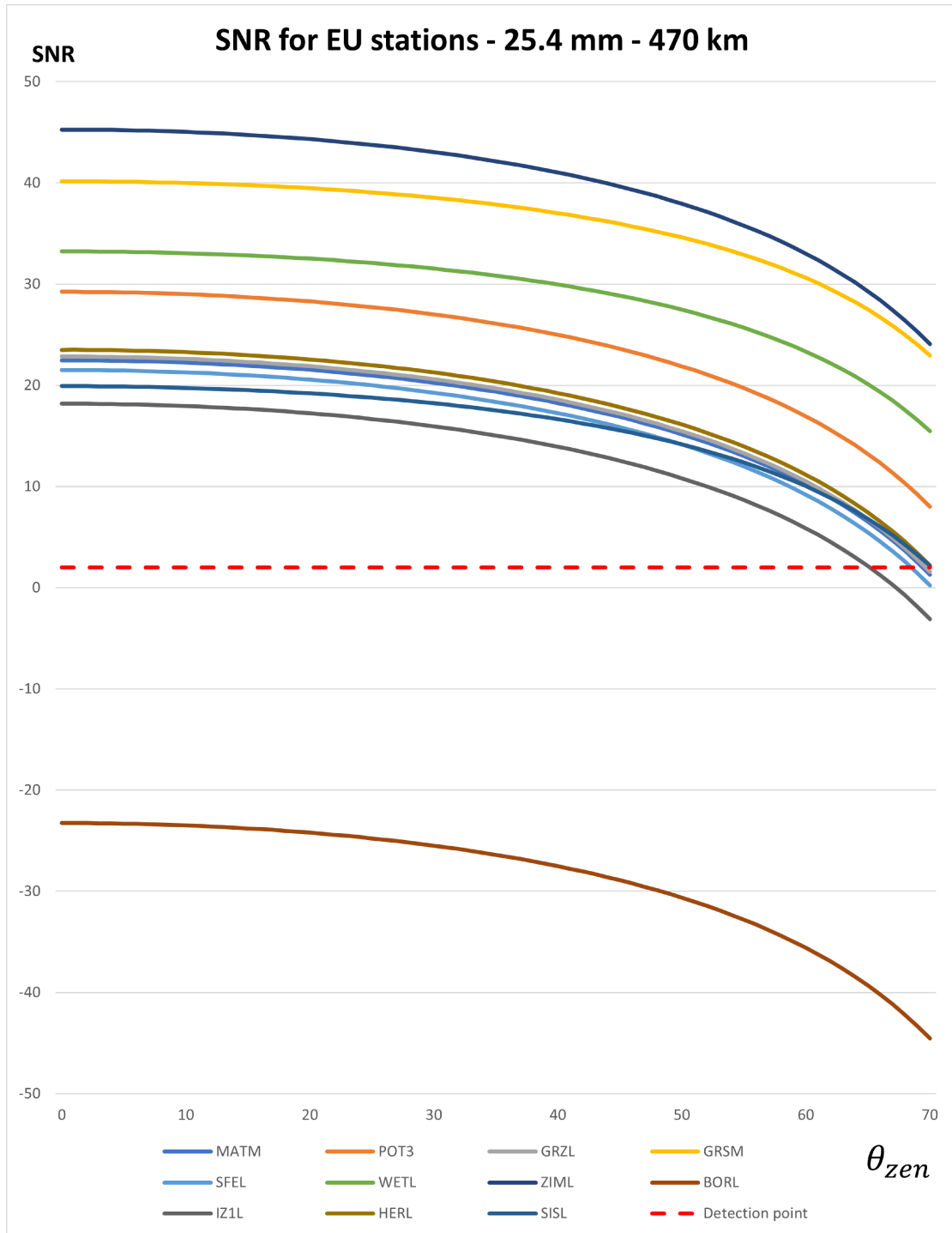
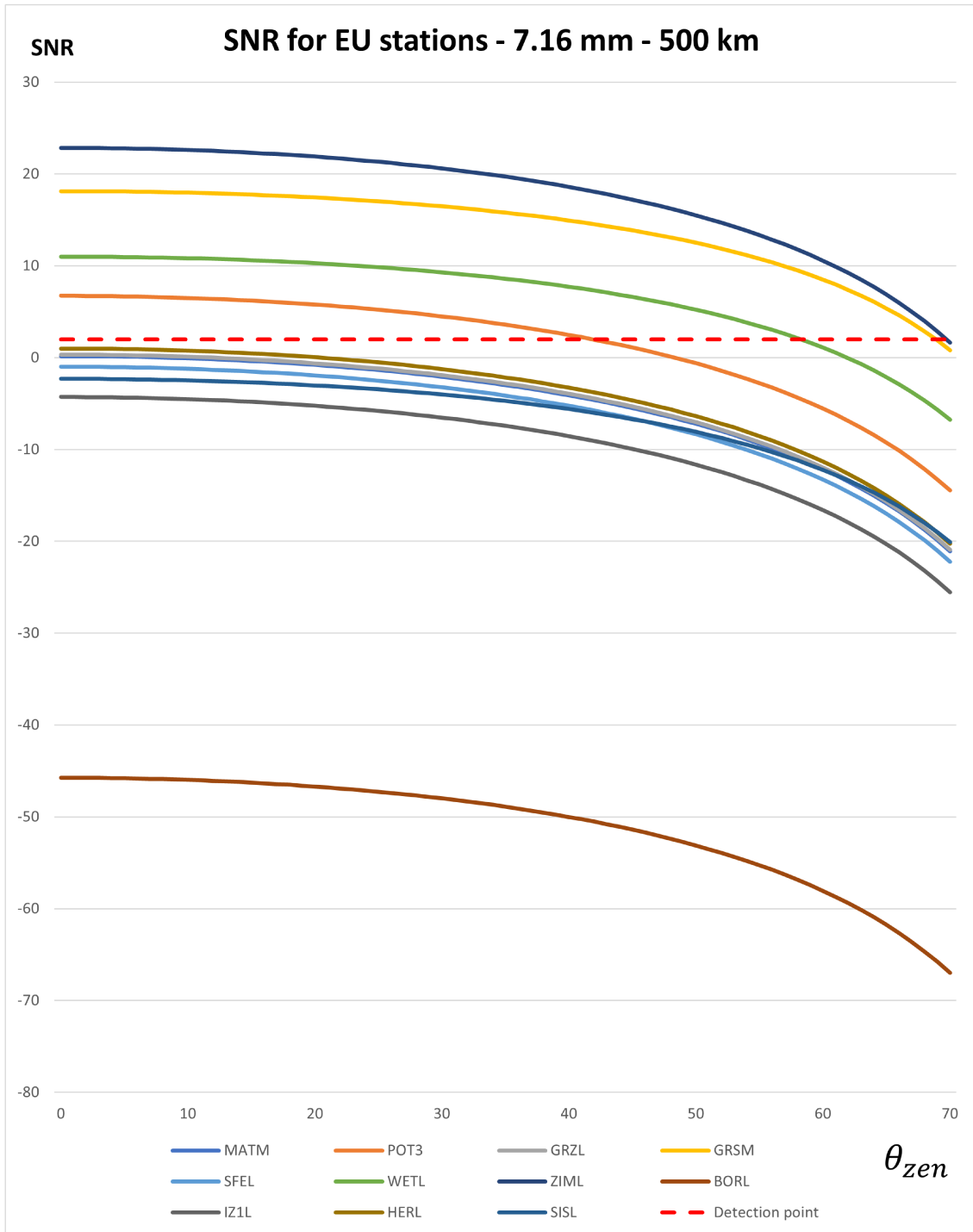Figure 3.16: SNR for EU stations for 25.4 mm diameter CCR - 470 km altitude.
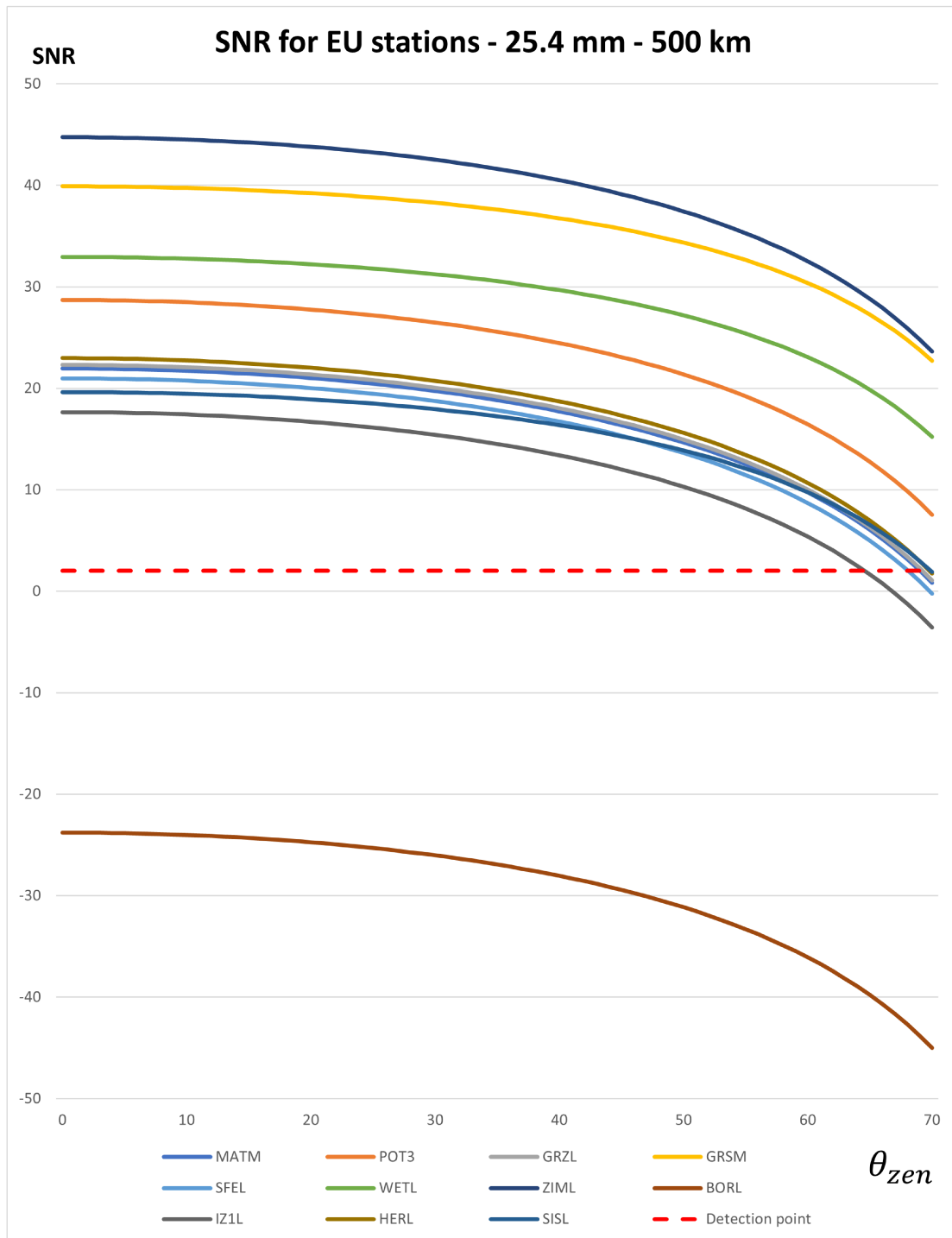
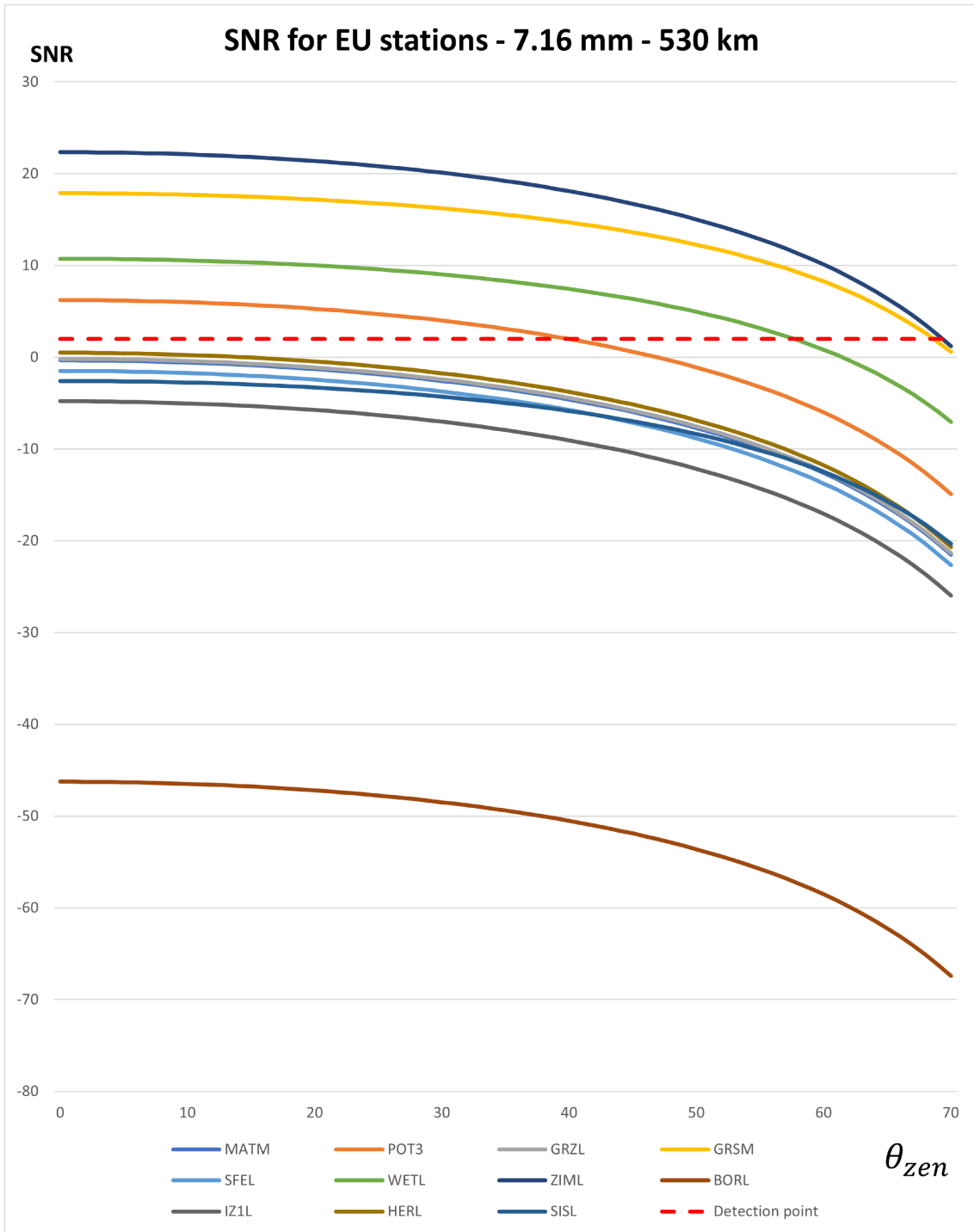Figure 3.17: SNR for EU stations for 25.4 mm diameter CCR - 500 km altitude.
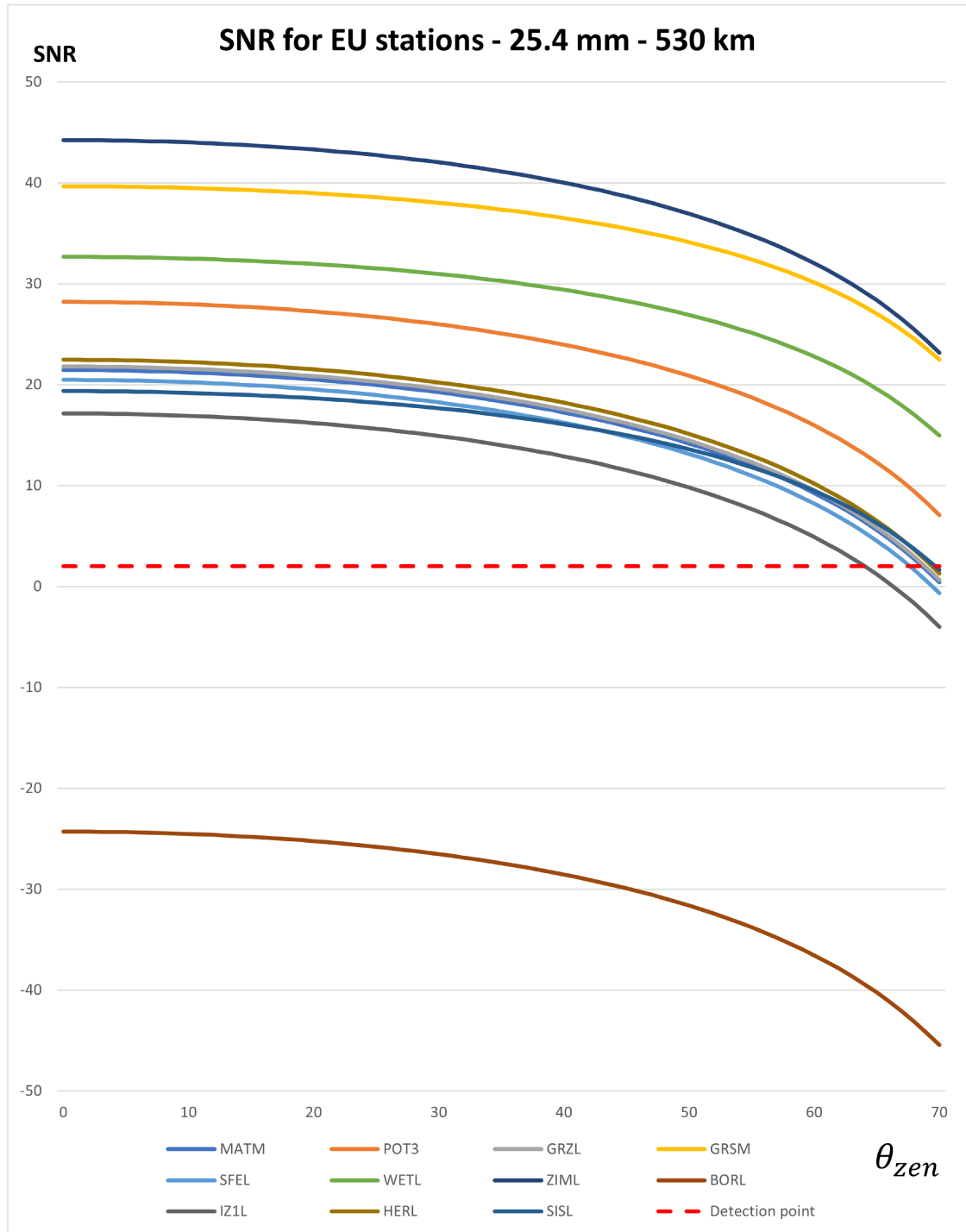
Figure 3.18: SNR for EU stations for 25.4 mm diameter CCR - 530 km altitude.
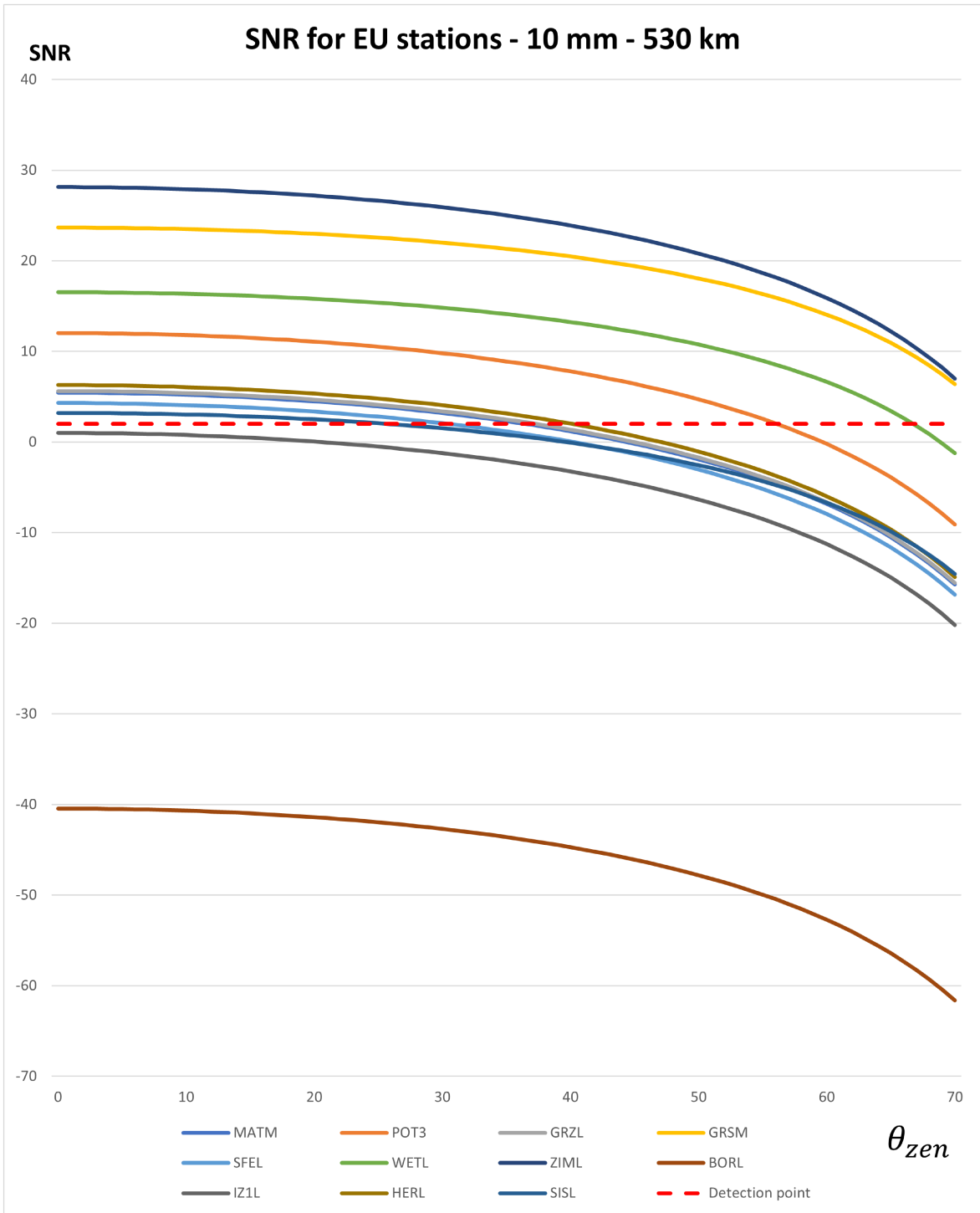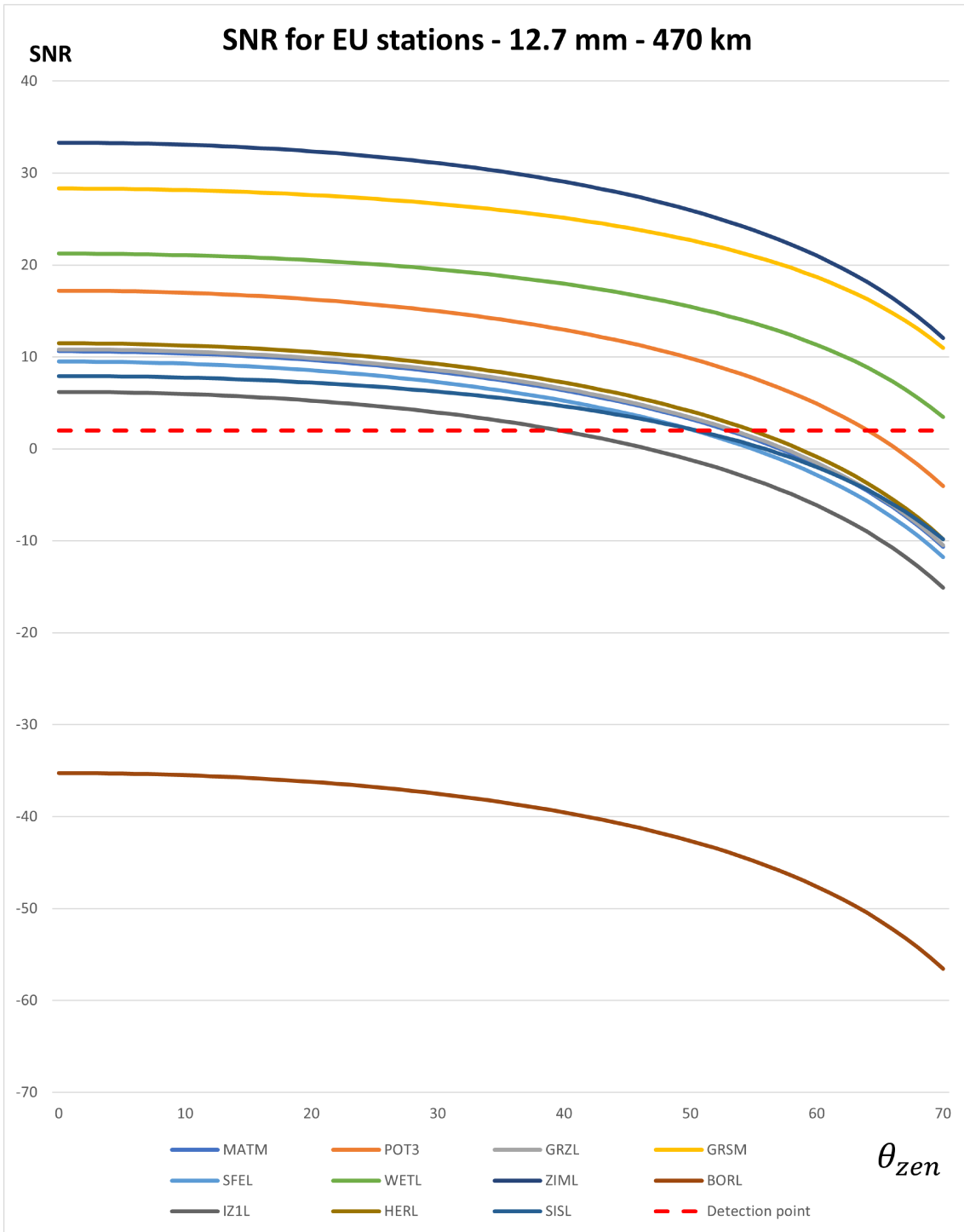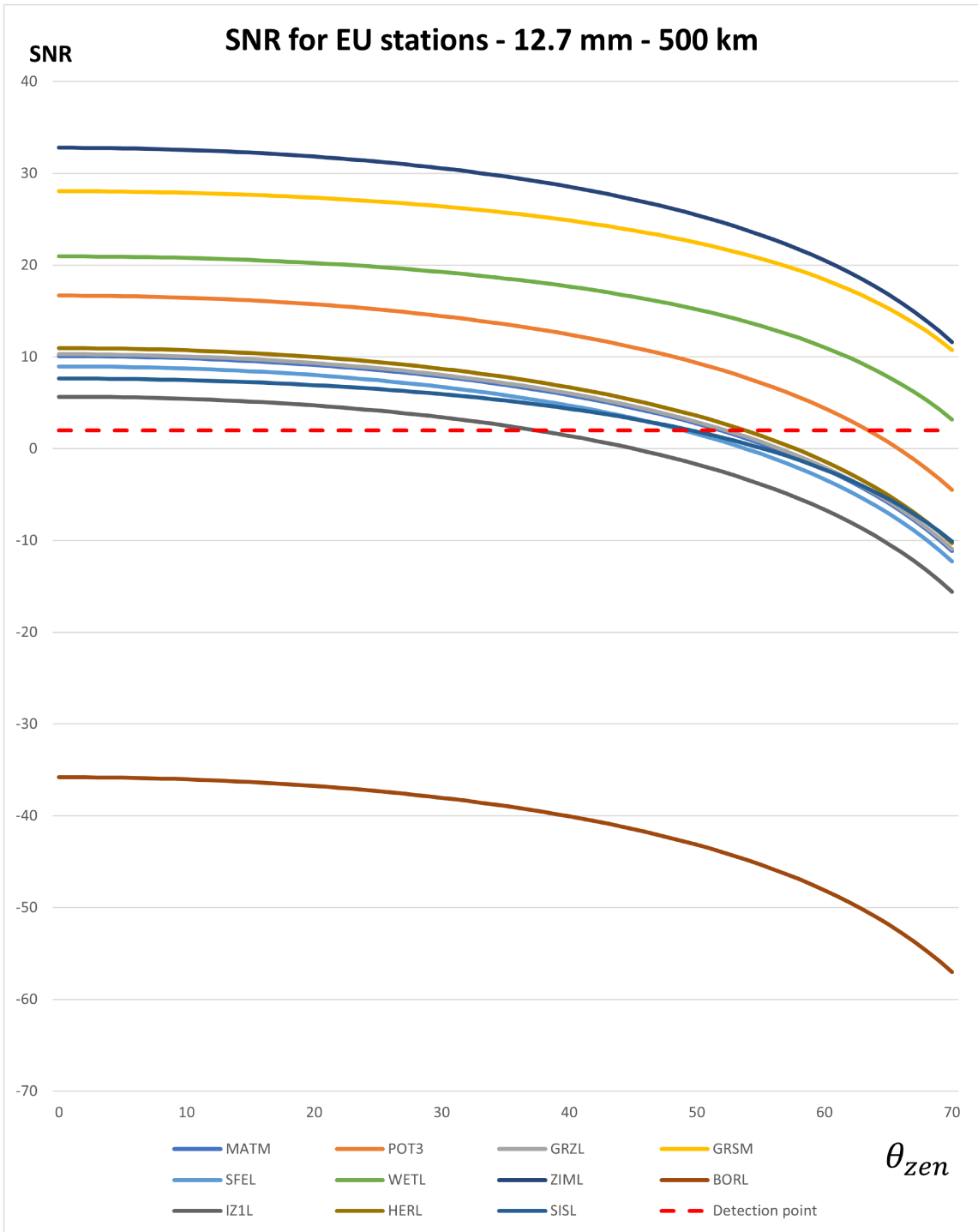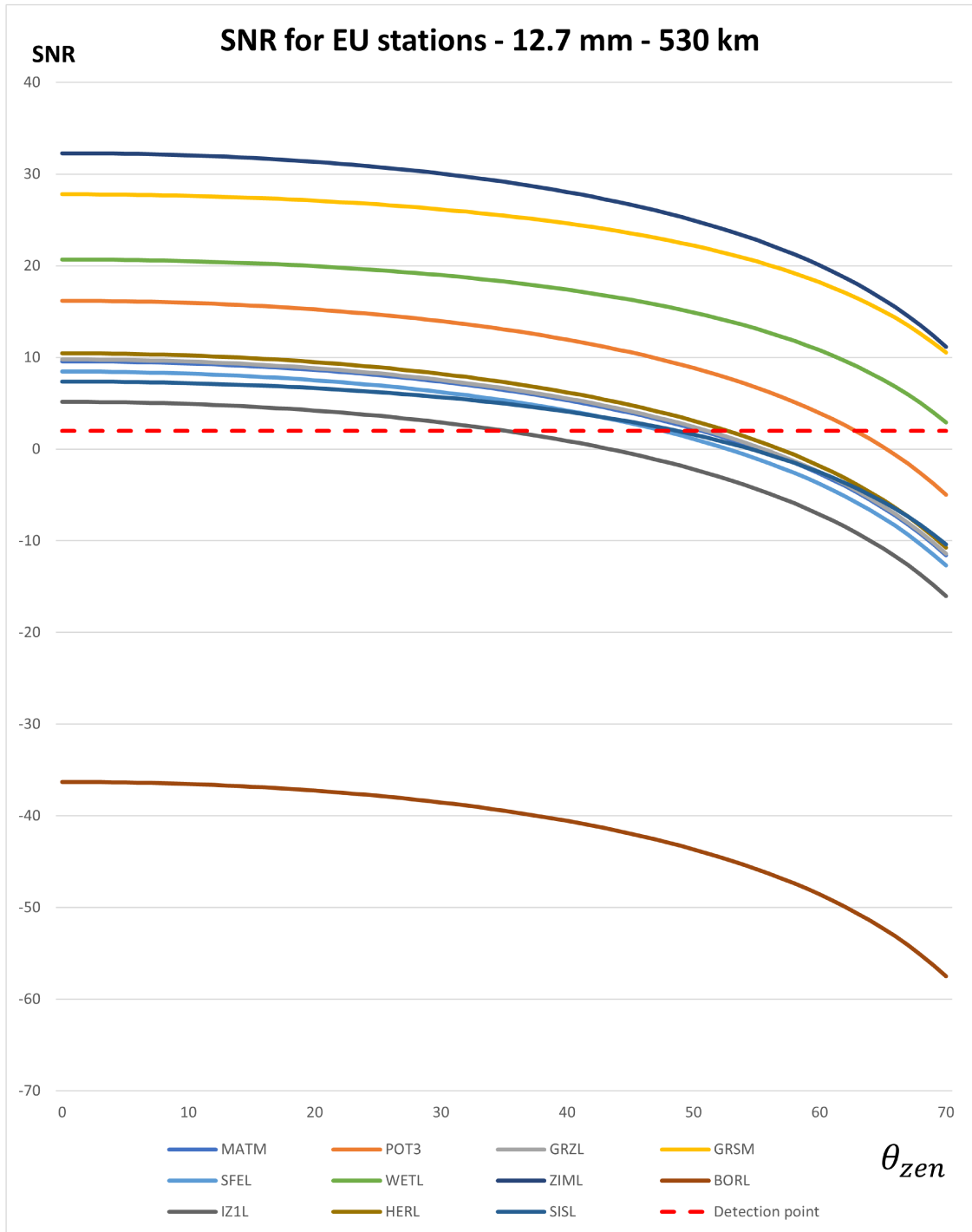
3.3.3 Visibility from ILRS stations

CCRs in multiple faces of the spacecraft extend the total FOV, giving more tracking time for ground stations during nominal operations but also increasing probability of tracking the spacecraft in case of loss of attittude control. In order to assess feasibility of having CCR in multiple faces of the spacecraft to be compliant with requirement PL-CCR-FKT-307, an orbital simulation was set up.

Assumptions and limitations

For this analysis, the spacecraft orbit is assumed to be affected by secular and periodic perturbations caused by Earth's geometry and atmospheric drag [22]. A nadir-pointing attitude with no error is assumed. The ground station is assumed to start pointing at the CCR immediately when it becomes visible. Tracking mount pointing errors are not considered. As a preliminary configuration 3 CCR are considered. No CCRs on the $-Z$, $-X$ and $+X$ faces are considered, because of dimensional constraints imposed by solar panels, the magnetometer and the impact sensor respectively. Table 3.12 describes CCR positioning, each CCR is assumed to be at the center of the face it's mounted on.

Table 3.12: CCRs positions and corresponding faces.

CCR ID	Position
1	$+Z$ face
2	$+Y$ face
3	$-Y$ face

Analysis description

The goal of the analysis is to evaluate when a CCR is within a station line of sight. Each CCR has a FOV half-angle of 30 deg. The projection of the CCR FOV on Earth surface is shown in Figure 3.7. The CCR is in sight and there is a pointing opportunity when the station is inside the projected FOV and satellite elevation seen from the station is over the minimum tracking elevation of the telescope mount. Minimum tracking elevation is a parameter publicly available on the ILRS site.

Figure 3.19: Station visibility simulation in MATLAB environment, CCR FOV projection is shown in green.

A tool from MATLAB Satellite Navigation Toolbox propagates the spacecraft orbit (using SGP4 propagator) with the given set of orbital parameters, then computes pointing opportunities duration with every ILRS station (stations coordinates are publicly available). The output is a table showing a series of events. Each event refers to a specific CCR in line of sight of a specific station, with starting epoch, ending epoch and duration. The chosen orbit for this analysis is a 500 km altitude SSO. Simulation parameters are summarized in Table 3.13.

Table 3.13: Simulation parameters.

Parameter	Value
h_{SAT}	500 km
i	96°
Start date and time	30/03/2027 00:00
Duration	1 month
Time step	10 s
θ_{CCR}	30°

Analysis results

The results show that every CCR in the proposed configuration is visible from the ground, with a mean duration of 65 seconds per pointing opportunity. The average number of pointing opportunities for any station is 36. The total pointing opportunities time is 28.3 hours, which is 3.9% of simulation time. Table 3.14 shows a summary of number of opportunities and average duration for each CCR, while Table 3.15 shows the same summary but for each ILRS station.

Table 3.14: Opportunities and average duration for CCRs.

CCR	Opportunities	Avg. Duration (s)
$+Z$	692	56
$+Y$	333	106
$-Y$	371	104

Results also show that detection of $-Y$ and $+Y$ CCRs is highly dependent on minimum tracking elevation for the telescope mount. Lateral CCRs show fewer tracking opportunities, most of them from stations with lower minimum elevation angles. For these opportunities the average tracking time is higher because of the wider projected FOV.

Table 3.15: Opportunities and average durations for ILRS stations.

Station	Opportunities	Avg. Duration (s)
MATM	18	53
POT3	24	48
GRZL	84	101
GRSM	82	101
SFEL	52	78
WETL	20	53
ZIML	23	51
BORL	22	54
IZ1L	17	50
HERL	22	56
SISL	36	60
STL3	30	56
SHA2	68	100
KUN2	42	73
HRTL	16	51
HARL	16	51
BRAL	16	52
SJUL	46	75
AREL	15	54
JFNL	66	102
SEJL	18	49
GMSL	16	55
BEIL	107	138
THTL	15	53
HA4T	18	45
MONL	18	50
GODL	51	74
YARL	45	73
KTZL	20	55
IRKL	25	52
BADL	24	53
ZELL	21	48
SVELL	31	53
BAIL	18	53
ARKL	114	136
RIGL	48	54
ALTL	23	53
MDVS	23	56
SIML	46	65

3.4 Attitude determination accuracy assessment

As a preliminary assessment of obtainable attitude determination accuracy and compliance with requirement PL-CCR-PRF-308, a measurement simulation was set up in MATLAB.

3.4.1 Assumptions and limitations

For this analysis, the spacecraft orbit is assumed to be affected by secular and periodic perturbations caused by Earth's geometry and atmospheric drag. The spacecraft attitude is simulated considering torques and errors from ADCS and real geometry and mass. CCR detection is assumed to be happening constantly and consistently through measurements. CCR return signals are assumed to be clearly distinguished and each return signal is assumed to be associated with the CCR that reflected it. Laser ranging measurements are assumed to be affected by an RMS error of 2.5 mm when assuming a kHz laser system and 1 cm when assuming a sub-kHz system [13].

Attitude determination method The following method to obtain incidence angles was proposed from [17] and [18]. The geometrical model is shown in Figure 3.8.
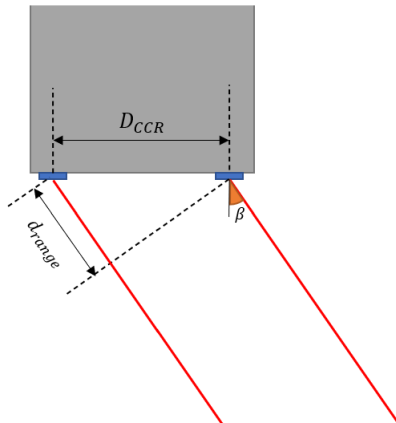
Figure 3.20: Geometrical model of the method.

The 4 CCRs on the $+Z$ face of the spacecraft are split in 2 groups formed by couples of CCRs (1-2, 3-4 and 2-4, 1-3). Each group is associated with an axis of rotation, respectively roll and pitch. To compute incident roll and pitch angles, mean values for each couple of CCRs are computed in order to isolate the axis rotation. These mean values are subtracted in order to find the range difference d_{range} . Then, incident angle is computed as

$$\beta = arcsin \left(\frac{d_{range}}{D_{CCR}} \right) \qquad (3.24)$$

where d_{range} is the range difference and D_{CCR} is the baseline distance.

49

3.4.2 Analysis description

The simulation represents a scenario of a pass over a ground station. Two cases are considered: one with positional accuracy 2.5 mm, representing a kHz system, and the other with positional accuracy of 1 cm, representing a sub-kHz system. A random error with normal deviation as the accuracy is added to the computed measurements, simulating real accuracy. Attitude is simulated through the AlbaSat system simulator from the Mission Analysis team, done in Simulink, in a nominal nadir pointing attitude control mode. The simulator's output is a table with quaternions for every step of the simulation. The spacecraft is on a 500 km SSO, passing over Graz station. A tool from MATLAB Satellite Communications Toolbox computes "real" range to every CCR, then the measure error is added. Incident angles are computed with the described method and compared with angles obtained without the measure error. For this analysis a CCR baseline distance of 62 mm is considered.

Table 3.16: Simulation parameters.

Parameter	Value
h_{SAT}	500 km
i	96°
Start date and time	30/03/2027 23:00:30
Duration	80 s
Time step	0.1 s
D_{CCR}	62 mm
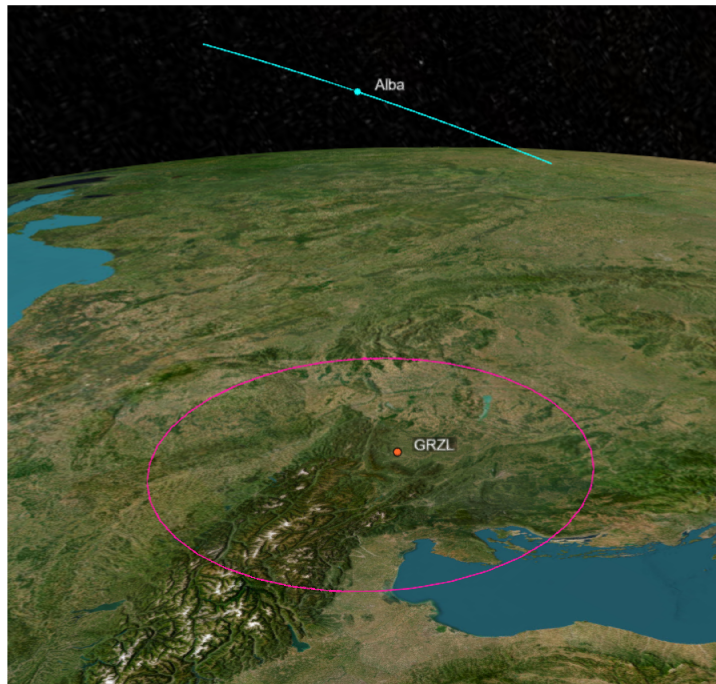
Figure 3.21: Attitude determination accuracy assessment scenario.

3.4.3 Analysis results

The following graphs show measured incident angle values (in blue) compared to nomimal values (in red) and delta between them for the kHz system scenario. RMS delta are 2.41 deg for pitch and 2.29 deg for roll.
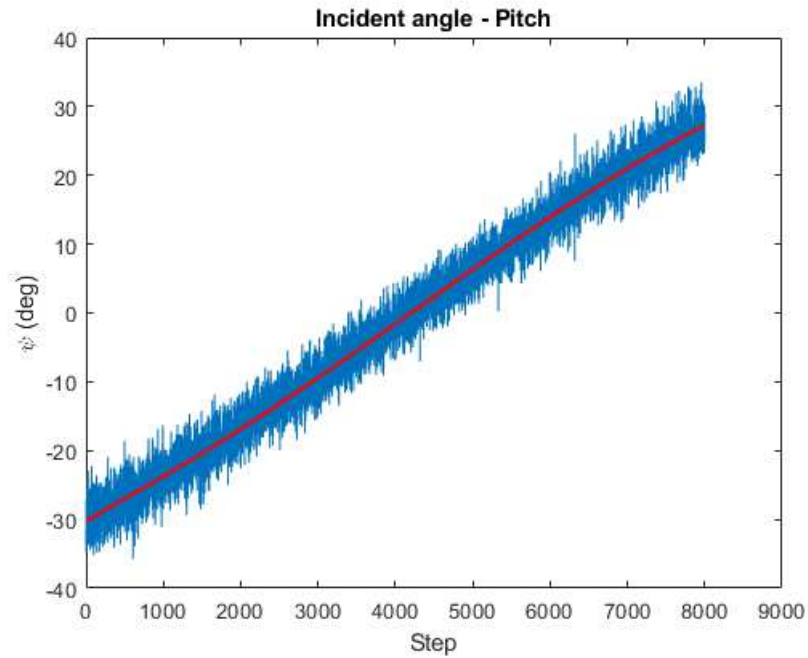
Figure 3.22: Pitch incident angle obtained from a kHz system.
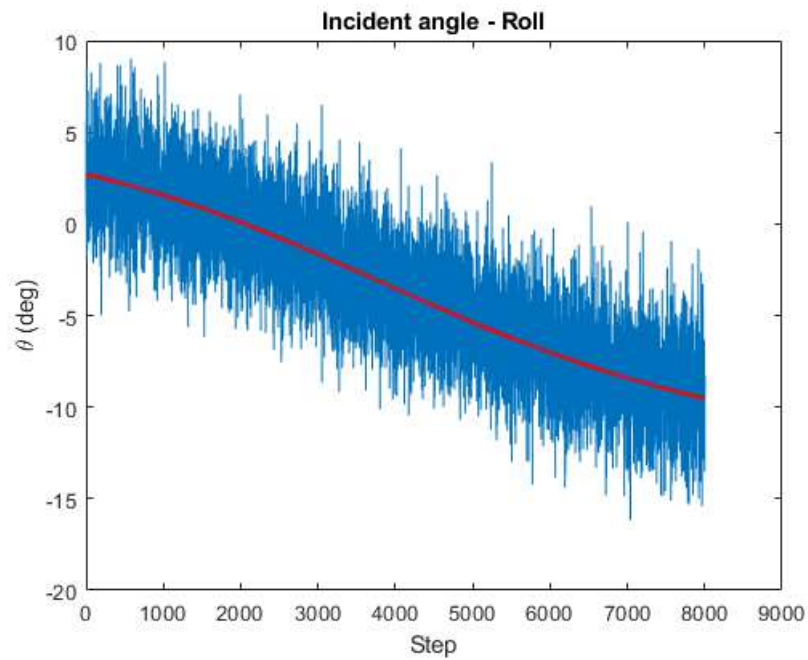
Figure 3.23: Roll incident angle obtained from a kHz system.
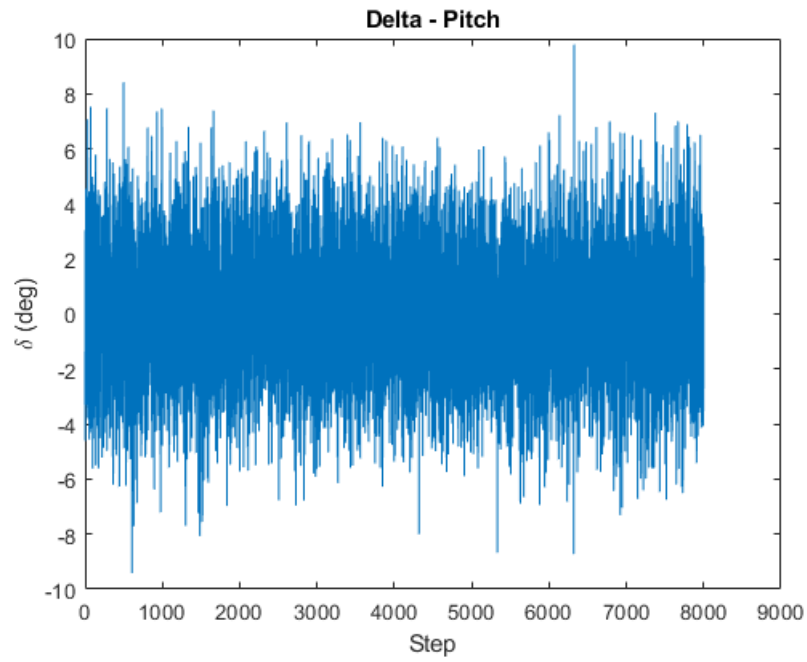
Figure 3.24: Difference between nominal and estimated pitch incident angle obtained from a kHz system.
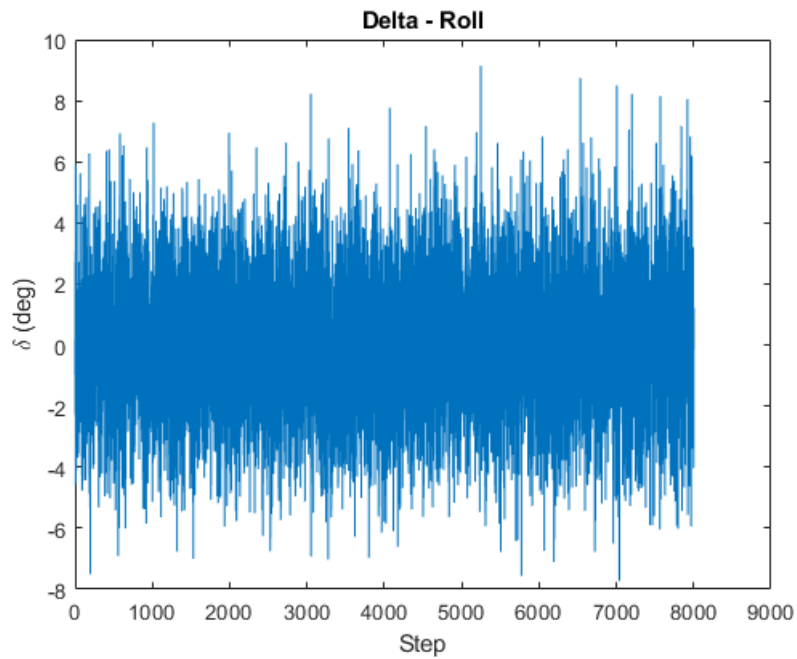
Figure 3.25: Difference between nominal and estimated roll incident angle obtained from a kHz system.

For a sub-kHz system delta increases to a RMS value of 9.99 deg for pitch and 9.42 deg for roll. Results are shown in the following graphs

52
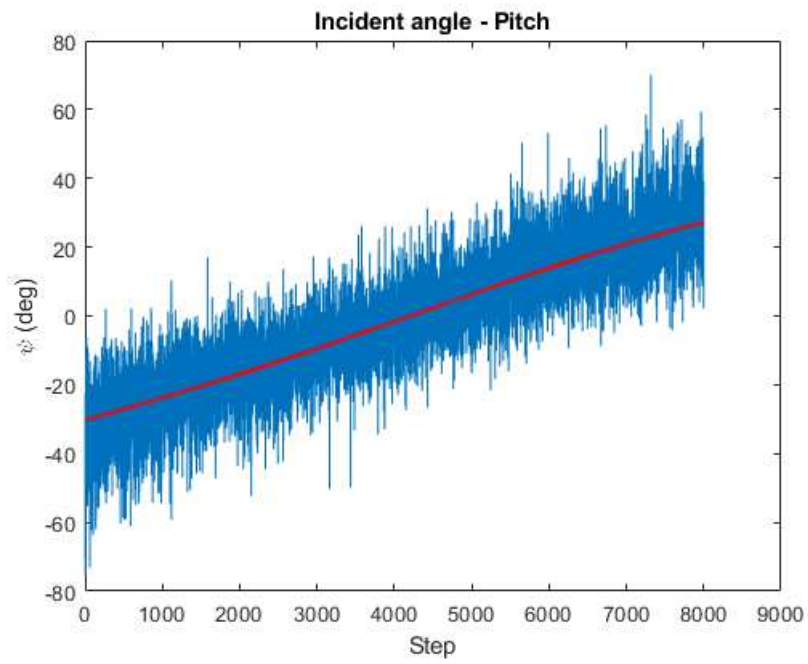
Figure 3.26: Pitch incident angle obtained from a sub-kHz system.
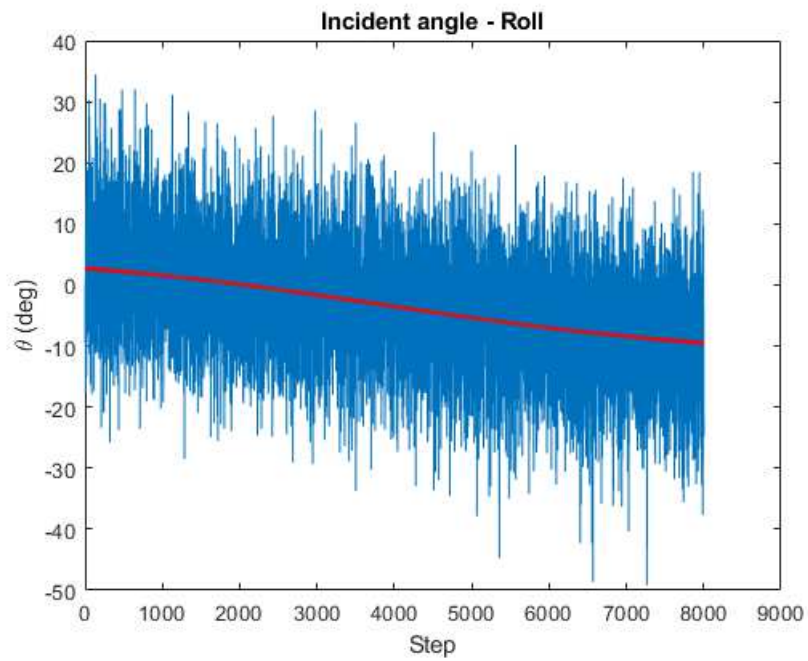
Figure 3.27: Roll incident angle obtained from a sub-kHz system.
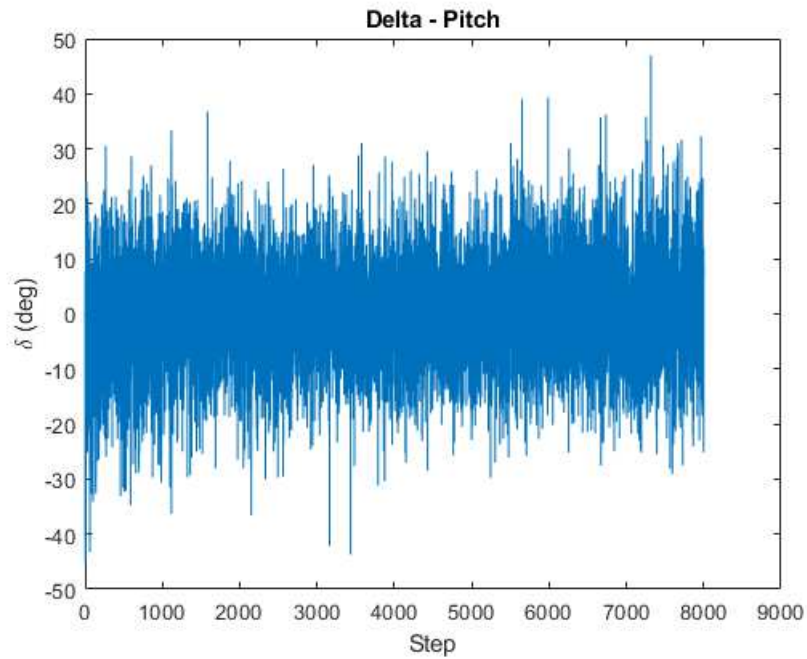
Figure 3.28: Difference between nominal and estimated pitch incident angle obtained from a sub-kHz system.
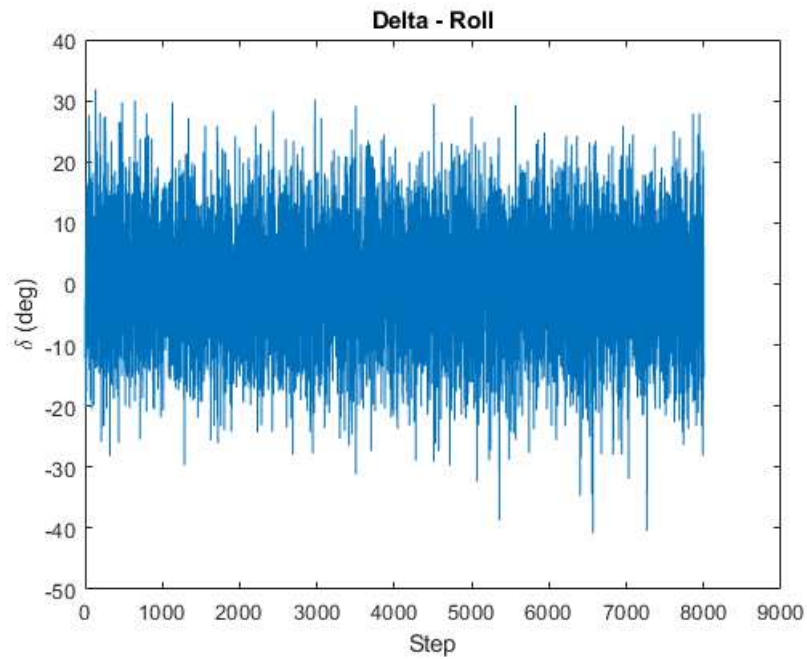
Figure 3.29: Difference between nominal and estimated roll incident angle obtained from a sub-kHz system.

The results show that the proposed CCR configuration on the $+Z$ face of the spacecraft can possibly allow incident angle measurements within the requirements. However this analysis is preliminar and must be further refined, as it assumes having clearly distinguished CCR traces and, most importantly, knowing which CCR every

54

trace belongs to. Also, operating modes of SLR detectors may not allow a simultaneous storage of the photons reflected by different retroreflectors. All these effects, together with return rate, will limit the applicability of the proposed algorithm and will be investigated in a further analysis.

3.5 Trade-off analysis

The whole performance analysis objective was to obtain information about CCR behaviour in most operative situations. This data, in addition to dimensional, mass and budget constraints, will eventually lead to a COTS component and a CCR configuration choice. In order to evaluate all of these factors with their respective weights, a trade-off analysis was done.

3.5.1 COTS components

In order to select a COTS component to use for this payload, the first thing to do is to choose the proper CCR diameter. Commercially available diameters considered for this payload are : 7.16 mm, 10 mm, 12.7 mm and 25.4 mm. This is done through a trade-off table, including signal return, size, mass and cost. As CCRs are cheap and light components, and there is no big difference in cost and mass between the 4 diameters, these parameters weight less in the choice. The main drivers of the choice are signal return strength and volume. Table 3.17 shows the trade-off analysis table. For each parameter a weight was decided and then for each CCR diameter a rating from 1 to 5 where 1 is the worst and 5 is the best was assigned for every criteria.

Table 3.17: Trade-off analysis.

CRITERIA	WEIGHT	7.16 mm RATING	7.16 mm TOTAL	10 mm RATING	10 mm TOTAL	12.7 mm RATING	12.7 mm TOTAL	25.4 mm RATING	25.4 mm TOTAL
SIGNAL RETURN	40.00%	1	0.4	3	1.2	4	1.6	5	2
MASS	10.00%	4	0.4	4	0.4	4	0.4	3	0.3
COST	20.00%	2	0.4	4	0.8	4	0.8	2	0.4
VOLUME	30.00%	5	1.5	3	0.9	3	0.9	1	0.3
	100.00%		2.7		3.3		3.7		3

The 12.7 mm diameter, showing significant improvement in signal strength with a relatively low increase in volume compared to the 10 mm CCR, is chosen for this payload. The 25.4 mm is clearly the one with best performance, but its dimensions can interfere with attitude determination operations, as the reduced baseline can cause return traces to overlap, making attitude determination impossible.

The final component choice is Thorlabs PS977-A TIR Retroreflector 12.7 mm [23]. As for the coating, the choice was determined by requirements PL-CCR-INT-305 and PL-CCR-PRF-306. Thorlabs offers and AR coating restricting wavelengths to the 350-700 nm range. Other options were considered, but this was the best for cost and availability.

3.5.2 CCR configuration

One of the main drivers of attitude determination accuracy is the baseline distance between CCRs. So, in order to get closer to the maximum obtainable accuracy, CCRs on the $+Z$ face must be placed the closest possible to the face vertices. Fortunately, the $+Z$ face is dedicated to the CCR and QPL payloads, so no dimensional constraints limit CCR placement apart from the CubeSat main structure.

CCRs placement on lateral faces is limited by various components. The $+X$ face is completely taken by the Impact Sensor, so no CCRs can be placed there. The $+Y$ and $-Y$ faces are mostly covered with solar panels, but at the interface between the 2 units of the CubeSat a few holes designed for sun-sensors and/or star trackers can accomodate one CCR. For the $-X$ face, this place is taken from the deployable magnetometer, so no CCR can be put there. The $-Y$ face can accomodate one CCR in the same way as the $+Y$ face. A CCR on the $-Z$ face could increase tracking opportunities in case of loss of attitude control. Unfortunately, the $-Z$ face is taken by a solar panel. The antenna chosen for AlbaSat, from the producer ISISPACE [24], has an aperture that could accomodate one CCR, and the P110UC-SUN solar panel from GOMSPACE [25] also has one, but the position of the power connectors makes them not compatible. The only possible choice is the P110C solar panel from GOMSPACE that has power connectors designed to have cables pass through the antenna aperture. This solar panel can't accomodate a CCR, so no CCRs can be put on the $-Z$ face.

Given these considerations, the proposed design is composed of 6 CCRs (TBC), a summary of the configuration is shown in Table 3.17.

Satellite face	N° of CCRs
$+Z$	4
$+Y$	1
$-Y$	1

Table 3.18: Proposed CCR configuration.

Conclusions and future work

In order to do orbit and attitude determination through laser ranging for the AlbaSat mission, a CCR payload was designed. First, from mission objectives and constraints a series of technical requirements was obtained, then a series of analyses was performed to determine the diameter, quantity and configuration on the spacecraft of commercial CCRs. The results shown that a design with 6 CCRs of 12.7 mm diameter placed on various faces of the spacecraft is compliant with the requirements. Table 3.18 shows the compliancy status and rationale for every requirement. An holding structure has been designed from the team and the 3D printed development model has been built and is now undergoing dimensional checks. The next design phases will include the refinement of the analyses, which could lead to an update on the design for the Engineering Model. This will be produced with the final materials and CCRs, will be representative of the final design and will undergo an environmental test campaign.
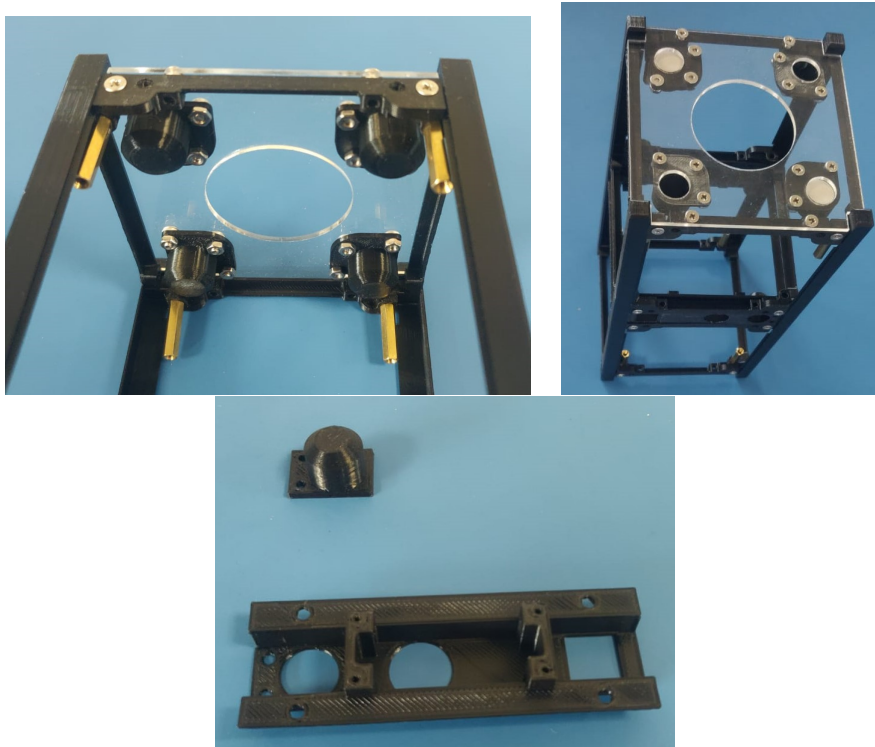
Figure 4.1: Development model assembly : detail of the 4 CCRs on the $+Z$ face (left, right) and detail of $+Y$ and $-Y$ mounting structure (low).

Table 4.1: Requirements compliancy table for the proposed design.

Requirement to be verified	Compliance status and rationale
SAT-FKT-301 The Cubesat shall return a laser beam	**Compliant at Phase C.** The CCRs will reflect a laser beam pointed to the Cubesat
PL-CCR-CON-303 The CCR payload shall be passive	**Compliant at Phase C.** The payload does not draw power from the EPS and has no moving parts
PL-CCR-INT-305 The payload shall be compatible with the use of ILRS infrastructure	**Compliant at Phase C.** The CCRs will reflect a 532 nm laser beam
PL-CCR-FKT-307 The payload shall grant the possibility to compute orbit determination in case of loss of attitude control	**Unknown at Phase C.** CCRs are put in multiple faces of the Cubesat. Further analysis required to evaluate visibility in case of tumbling satellite
PL-CCR-FKT-308 The CCRs on the +Z face shall allow attitude determination with an accuracy of minimum 30 deg.	**Compliant at Phase C.** 4 CCRs are positioned on the +Z face. Obtainable accuracy is 10 deg.

ILRS stations parameters

Station	Energy per pulse (mJ)	Repetition rate (Hz)	Pulse width (ps)	Detector efficiency	Transm. optics efficiency	Receiv. optics efficiency	Aperture (m)	Beam divergence (rad)	Pointing error (rad)	Beam diameter (m)	Filter width (nm)	Detector FOV (rad)	Range gate (ns)	Altitude
MATM	100	10	50	0.4	0.75	0.87	1.5	9.70E-06	4.85E-06	0.01	0.3	2.90E-04	20	536.9
POT3	0.7	2000	10	0.4	0.8	0.4	0.44	2.42E-05	2.42E-05	0.15	0.4	1.45E-04	50	123.5
GRZL	0.5	2000	10	0.2	0.7	0.3	0.5	2.42E-05	2.42E-05	0.06	0.3	9.70E-05	200	539.4
GRSM	200	10	120	0.2	0.45	0.22	1.54	4.85E-06	4.85E-06	1.54	0.12	3.39E-06	100	1323.1
SFEL	50	10	30	0.2	0.85	0.55	0.6	7.27E-05	7.27E-05	0.1	0.2	2.42E-04	200	98.2
WETL	0.2	500	10	0.8	0.5	0.5	0.75	2.78E-04	5.56E-04	0.75	0.2	2.42E-04	200	665
ZIML	8	110	60	0.18	0.85	0.5	1	4.85E-06	9.70E-06	0.15	0.1	4.36E-05	40	951.2
BORL	50	10	60	0.1	0.7	0.7	0.65	3.88E-05	4.85E-05	0.02	7	4.85E-05	300	123.4
IZI1	0.4	400	10	0.42	0.9	0.8	0.8	2.81E-05	2.42E-05	0.06	0.3	9.70E-05	0	2439.7
HERL	1	1000	10	0.2	0.7	0.7	0.5	2.42E-05	9.70E-06	0.03	0.15	9.70E-05	200	75
SISL	3	1000	30	0.15	0.59	0.44	0.75	2.91E-05	1.45E-05	0.75	1	4.85E-04	100	62.44
STL3	20	60	12	20	0.95	0.95	1	3.39E-05	6.79E-06	1	2	5.82E-05	200	805
SHA2	2	2000	45	0.3	0.5	0.15	0.6	3.88E-05	2.42E-05	0.05	0.15	9.70E-05	10	99.961
KUN2	1	1000	25	0.2	0.5	0.5	0.51	5.82E-05	2.42E-05	0.1	0.1	1.94E-04	168	1987.05
HRTL	2.5	300	300	0.1	0.66	0.5	0.25	4.85E-05	1.45E-05	0.03	0.1	9.70E-05	50	1414
HARL	100	10	200	0.133	0.94	0.76	0.762	1.45E-04	2.91E-06	0.093	100	2.91E-05	2000	1406.822
BRAL	2.5	300	200	0.1	0.6	0.6	0.25	4.85E-05	1.45E-05	0.03	0.1	9.70E-05	50	1029.24
SJUL	50	20	50	0.2	0.7	0.7	0.6	4.85E-04	2.42E-05	0.02	1000	2.91E-04	10	727.221
AREL	100	10	150	0.1312	0.7	0.4	0.28	9.70E-05	2.42E-05	0.093	1	1.45E-04	2000	2489.05
JFNL	0.9	1000	25	0.2	0.95	0.9	1	4.00E-04	9.70E-06	0.06	0.15	2.42E-04	10	76.7
SEIL	2.5	5000	50	0.12	0.923	0.649	0.4	2.42E-05	2.42E-05	0.08	0.27	4.36E-04	100	176.415
GMSL	250	10	250	0.12	0.5	0.5	1	1.45E-05	9.70E-06	0.8	0.38	5.82E-04	1000	141.0967
BEIL	2.5	1000	25	0.2	0.7	0.7	0.6	4.99E-04	2.42E-05	0.01	0.2	5.82E-05	10	82.3
THTL	100	10	200	0.1312	0.94	0.76	0.762	1.45E-04	2.91E-05	0.093	100	2.91E-05	2000	82.171
HAAT	100	10	150	0.1312	0.7	0.4	0.28	9.70E-05	2.42E-05	0.093	1	2.91E-05	2000	3056.272
MONL	100	10	150	0.1312	0.7	0.73	0.762	9.70E-05	2.91E-05	0.093	10	2.91E-05	600	1842.177
GODL	100	10	150	0.133	0.7	0.54	0.762	9.70E-05	1.75E-05	0.093	1	2.91E-05	2000	19.184
YARL	100	10	150	0.155	0.75	0.54	0.760	6.79E-05	3.39E-06	0.085	1	4.36E-04	1000	244
KTZL	100	10	250	0.05	0.37	0.16	1	1.94E-04	1.45E-05	0.250	0.2	2.42E-04	200	68.7
IRKL	2.5	300	250	0.1	0.7	0.5	0.25	4.85E-05	1.45E-05	0.03	0.1	2.91E-05	50	505.62
BADL	2.5	300	300	0.1	0.6	0.5	0.25	9.70E-05	1.45E-05	0.03	0.1	9.70E-05	50	803.3
ZELL	2.5	300	300	0.1	0.6	0.5	0.25	4.85E-05	1.45E-05	0.03	0.1	9.70E-05	50	1155.4
SVELL	2.5	300	35	0.1	0.6	0.5	0.25	9.70E-05	1.45E-05	0.03	0.1	9.70E-05	50	69
BAIL	2.5	300	300	0.1	0.6	0.6	0.6	9.70E-05	1.45E-05	0.03	0.1	9.70E-05	50	98.3
ARKL	2.5	300	300	0.1	0.6	0.5	0.25	4.85E-05	1.45E-05	0.03	0.1	9.70E-05	50	2077
RIGL	120	10	130	0.18	0.6	0.3	1	9.70E-05	2.42E-05	0.85	0.93	1.45E-04	20	31.3367
ALTL	2.5	300	150	0.1	0.6	0.3	0.6	4.85E-05	4.85E-05	0.04	0.1	9.70E-05	50	270
MDVS	2.5	300	300	0.1	0.5	0.5	0.25	4.85E-05	4.85E-05	0.03	0.1	9.70E-05	50	229.053
SIML	80	10	150	0.12	0.7	0.3	1	1.94E-05	4.85E-06	0.3	1000	9.70E-05	500	361.2

MATLAB code

B.1 Link budget

```matlab
1  clear
2  clc
3  close all
4
5  data = readtable('GS_data.xlsx');
6
7  lambda = 5.32E-07;                        % wavelenght
8  hv = 3.73E-19;                            % single photon energy
9  alt_alba = 530000;                        % stellite altitude
10 CCR_diam = 25.4E-03;                      % CCR diameter
11 N_bg_day = 1.4E+08;                       % background noise sunlit
       clouds
12 N_bg_night = 3E-06;                       % background noise at night
13
14 filename = 'Link_25.4_530km_FOV30.xlsx';
15
16 OCS_peak = 0.78*(pi^3*(CCR_diam^4))/(4*(lambda^2));
                      % peak optical cross section
17
18 E_t = (data.Energy./1000)./(hv);
                      % laser pulse energy
19 n = data.n_q.*data.n_t.*data.n_r;
                      % efficiencies
20 G_t = (2./((data.theta_D./2).^2)).*exp((...
21     data.theta_P./(data.theta_D./2)).^2);
                      % transmitter gain
22 A_r = (pi.*(data.Aperture./2).^2);
                      % receiver area
23
24 omega_r = (data.FOV./2).^2;
                      % receiver solid angle FOV
25
26 N_b_day = (data.n_q./hv).*N_bg_day.*(data.lambda_bp.*1E-09).*...
27     omega_r.*A_r.*data.n_r.*(data.rangeGate.*1E-09);
                      % photons from noise (day)
28 N_b_night = (data.n_q./hv).*N_bg_night.*(data.lambda_bp.*1E-09).*...
29     omega_r.*A_r.*data.n_r.*(data.rangeGate.*1E-09);
                      % photons from noise (night)
```

```
30 P_FA_day = 1-exp(-N_b_day);
                        % probability of false alarm (day)
31 P_FA_night = 1-exp(-N_b_night);
                        % probability of false alarm (night)
32
33 step = 1;
34 Ph = zeros(71,height(data));
35 P_PD = zeros(71,height(data));
36 P_SD_day = zeros(71,height(data));
37 P_SD_night = zeros(71,height(data));
38
39 angle = zeros(62,1);
40
41
42 for i = 90:-1:60
43     angle(step) = i;
44     zen = deg2rad(90-i);
                        % zenith angle and incidence angle
45     R = height2range(alt_alba,data.Elevation,i);
                        % slant range
46     theta_ref = asin(sin(zen)/1.455);
                        % internal refracted angle
47     mu = sqrt(1-(tan(theta_ref))^2);
48     eta_ocs = (2/pi)*(asin(mu)-(sqrt(2)*tan(theta_ref))*cos(zen));
                        % cross section reduction factor
49     OCS = (eta_ocs^2)*OCS_peak;
                        % OCS for incidence angle
50     rng = (1./(4.*pi.*R.^2)).^2;
                        % two way space loss
51     T_c = exp(-0.14*(1.341*sec(zen))^2);
                        % one way cirrus loss
52     T_a_AVG = exp(-0.25.*1.2.*sec(zen).*exp(-(data.Elevation./1000)
    ./1.2));            % one way atmospheric loss
53     T_a_BEST = exp(-0.18.*1.2.*sec(zen).*exp(-(data.Elevation
    ./1000)./1.2));
54     T_a_WORST = exp(-0.46.*1.2.*sec(zen).*exp(-(data.Elevation
    ./1000)./1.2));
55     Ph_BEST(step,:) = E_t.*n.*G_t.*A_r.*T_a_BEST.^2.*OCS.*rng';
                            % link equation
56     Ph_WORST(step,:) = E_t.*n.*G_t.*A_r.*T_a_WORST.^2.*T_c.^2.*OCS
    .*rng';
57     Ph_AVG(step,:) = E_t.*n.*G_t.*A_r.*T_a_AVG.^2.*T_c.^2.*OCS.*rng
    ';
58     N_BEST = Ph_BEST(:,:)+N_b_day';
                                    % total number of photoelectron (day
    )
59     N_WORST = Ph_WORST(:,:)+N_b_day';
60     N_AVG = Ph_AVG(:,:)+N_b_day';
61     P_PD_night_BEST(step,:) = 1-exp(-Ph_BEST(step,:));
                                    % probability of signal+noise
    detection (night)
62     P_PD_night_WORST(step,:) = 1-exp(-Ph_WORST(step,:));
63     P_PD_night_AVG(step,:) = 1-exp(-Ph_AVG(step,:));
64     P_PD_day_BEST(step,:) = 1-exp(-N_BEST(step,:));
                                    % probability of signal+noise
    detection (day)
```

```matlab
65    P_PD_day_WORST(step,:) = 1-exp(-N_WORST(step,:));
66    P_PD_day_AVG(step,:) = 1-exp(-N_AVG(step,:));
67    P_SD_day_BEST(step,:) = (1-P_FA_day').*P_PD_day_BEST(step,:);
                                   % probability of signal detection
   from noise (day)
68    P_SD_day_WORST(step,:) = (1-P_FA_day').*P_PD_day_WORST(step,:);
69    P_SD_day_AVG(step,:) = (1-P_FA_day').*P_PD_day_AVG(step,:);
70    P_SD_night_BEST(step,:) = (1-P_FA_night').*P_PD_night_BEST(step
   ,:);                             % probability of signal detection
   from noise (night)
71    P_SD_night_WORST(step,:) = (1-P_FA_night').*P_PD_night_WORST(
   step,:);
72    P_SD_night_AVG(step,:) = (1-P_FA_night').*P_PD_night_AVG(step
   ,:);
73    step = step+1;
74 end

75
76 for i = 30:-1:20
77    angle(step) = i;
78    zen = deg2rad(90-i);
                        % zenith angle and incidence angle
79    theta_inc = deg2rad(i);
80    R = height2range(alt_alba,data.Elevation,i);
                        % slant range
81    theta_ref = asin(sin(theta_inc)/1.455);
                        % internal refracted angle
82    mu = sqrt(1-(tan(theta_ref))^2);
83    eta_ocs = (2/pi)*(asin(mu)-(sqrt(2)*tan(theta_ref))*cos(
   theta_inc));                 % cross section reduction factor
84    OCS = (eta_ocs^2)*OCS_peak;
                        % OCS for incidence angle
85    rng = (1./(4.*pi.*R.^2)).^2;
                        % two way space loss
86    T_c = exp(-0.14*(1.341*sec(zen))^2);
                        % one way cirrus loss
87    T_a_AVG = exp(-0.25.*1.2.*sec(zen).*exp(-(data.Elevation./1000)
   ./1.2));                % one way atmospheric loss
88    T_a_BEST = exp(-0.18.*1.2.*sec(zen).*exp(-(data.Elevation
   ./1000)./1.2));
89    T_a_WORST = exp(-0.46.*1.2.*sec(zen).*exp(-(data.Elevation
   ./1000)./1.2));
90    Ph_BEST(step,:) = E_t.*n.*G_t.*A_r.*T_a_BEST.^2.*OCS.*rng';
                           % link equation
91    Ph_WORST(step,:) = E_t.*n.*G_t.*A_r.*T_a_WORST.^2.*T_c.^2.*OCS
   .*rng';
92    Ph_AVG(step,:) = E_t.*n.*G_t.*A_r.*T_a_AVG.^2.*T_c.^2.*OCS.*rng
   ';
93    N_BEST = Ph_BEST(:,:)+N_b_day';
                                   % total number of photoelectron (day
   )
94    N_WORST = Ph_WORST(:,:)+N_b_day';
95    N_AVG = Ph_AVG(:,:)+N_b_day';
96    P_PD_night_BEST(step,:) = 1-exp(-Ph_BEST(step,:));
                                   % probability of signal+noise
   detection (night)
97    P_PD_night_WORST(step,:) = 1-exp(-Ph_WORST(step,:));
```

```matlab
 98        P_PD_night_AVG(step,:) = 1-exp(-Ph_AVG(step,:));
 99        P_PD_day_BEST(step,:) = 1-exp(-N_BEST(step,:));
                                    % probability of signal+noise
      detection (day)
100        P_PD_day_WORST(step,:) = 1-exp(-N_WORST(step,:));
101        P_PD_day_AVG(step,:) = 1-exp(-N_AVG(step,:));
102        P_SD_day_BEST(step,:) = (1-P_FA_day').*P_PD_day_BEST(step,:);
                                    % probability of signal detection
      from noise (day)
103        P_SD_day_WORST(step,:) = (1-P_FA_day').*P_PD_day_WORST(step,:);
104        P_SD_day_AVG(step,:) = (1-P_FA_day').*P_PD_day_AVG(step,:);
105        P_SD_night_BEST(step,:) = (1-P_FA_night').*P_PD_night_BEST(step
      ,:);                         % probability of signal detection
      from noise (night)
106        P_SD_night_WORST(step,:) = (1-P_FA_night').*P_PD_night_WORST(
      step,:);
107        P_SD_night_AVG(step,:) = (1-P_FA_night').*P_PD_night_AVG(step
      ,:);
108        step = step+1;
109 end
110
111
112 var = data.Station';
113 Ph = array2table(Ph);
114 Ph.Properties.VariableNames = var;
115 P_SD_day_BEST = array2table(P_SD_day_BEST);
116 P_SD_day_BEST.Properties.VariableNames = var;
117 P_SD_day_WORST = array2table(P_SD_day_WORST);
118 P_SD_day_WORST.Properties.VariableNames = var;
119 P_SD_day_AVG = array2table(P_SD_day_AVG);
120 P_SD_day_AVG.Properties.VariableNames = var;
121 P_SD_night_BEST = array2table(P_SD_night_BEST);
122 P_SD_night_BEST.Properties.VariableNames = var;
123 P_SD_night_WORST = array2table(P_SD_night_WORST);
124 P_SD_night_WORST.Properties.VariableNames = var;
125 P_SD_night_AVG = array2table(P_SD_night_AVG);
126 P_SD_night_AVG.Properties.VariableNames = var;
127
128 angle = 90-angle;
129
130 writematrix(angle,filename,'Sheet','NIGHT BEST','Range','A2');
131 writematrix(angle,filename,'Sheet','NIGHT WORST','Range','A2');
132 writematrix(angle,filename,'Sheet','NIGHT AVG','Range','A2');
133 writematrix(angle,filename,'Sheet','DAY BEST','Range','A2');
134 writematrix(angle,filename,'Sheet','DAY WORST','Range','A2');
135 writematrix(angle,filename,'Sheet','DAY AVG','Range','A2');
136
137 writetable(P_SD_night_BEST,filename,'Sheet','NIGHT BEST','Range','
      B1');
138 writetable(P_SD_night_WORST,filename,'Sheet','NIGHT WORST','Range',
      'B1');
139 writetable(P_SD_night_AVG,filename,'Sheet','NIGHT AVG','Range','B1'
      );
140 writetable(P_SD_day_BEST,filename,'Sheet','DAY BEST','Range','B1');
141 writetable(P_SD_day_WORST,filename,'Sheet','DAY WORST','Range','B1'
      );
```

```
142 writetable(P_SD_day_AVG,filename,'Sheet','DAY AVG','Range','B1');
```

B.2   Power budget

```
1  clear
2  clc
3  close all
4
5  data = readtable('GS_data.xlsx');
6
7  filename = 'Power_25.4_530km.xlsx';
8
9  lambda = 5.32E-07;
                     % wavelenght
10 h = 530000;
                     % satellite altitude
11 CCR_diam = 25.4E-03;
                     % CCR diameter
12
13
14 P_avg = (data.Energy.*1E-03).*data.RepetitionRate;
                     % average laser power
15 duty_cycle = (data.PulseWidth.*1E-12).*data.RepetitionRate;
                     % duty cycle
16 P_peak = P_avg./duty_cycle;
                     % peak power
17
18 step = 1;
19 trasm_up = zeros(71,height(data));
20 trasm_down = zeros(71,height(data));
21 trasm_tot = zeros(71,height(data));
22
23 P_b = 1.48E08.*((data.FOV./2).^2).*pi.*((data.Aperture./2).^2).*...
                     % Power from noise
24     (data.lambda_bp.*1E-09);
25
26
27 angle = zeros(71,1);
28
29 for i = 90:-1:20
30     angle(step) = i;
31     R = height2range(h,data.Elevation,i);
                     % slant range
32     zen = deg2rad(90-i);
                     % zenith angle
33     n_0_up = 0.2.*data.n_t.*10^(-(4.34*0.8*sec(zen))/10);
34     n_0_down = 0.2.*data.n_r.*10^(-(4.34*0.8*sec(zen))/10);
35
36     % Uplink beam diameter
37     w_z_up = data.BeamDiameter.*sqrt(1+((R'.*lambda)./(pi.*(data.
    BeamDiameter).^2).^2));
```

66

```
38
39      % Uplink transmittance
40      trasm_up(step,:) = n_0_up.*(1-exp(-2.*CCR_diam^2./w_z_up.^2));
41
42      % Downlink beam diameter
43      w_z_down = CCR_diam*sqrt(1+((R'*lambda)./(pi*(CCR_diam)^2)^2));
44
45      % Downlink transmittance
46      trasm_down(step,:) = n_0_down.*(1-exp(-2.*data.Aperture.^2./
    w_z_down.^2));
47
48      step = step+1;
49  end
50
51  trasm_tot = trasm_up.*trasm_down;
52
53  P_return_avg = P_avg'.*trasm_tot.*1E+9; % return avg power in
        nanowatts
54  P_return_peak = P_peak'.*trasm_tot;
55
56  SNR = 10*log10((P_return_avg.*1E-9)./(P_b'));
57
58  MIN = min(SNR(:,1))
59
60  MAX = max(SNR(:,1))
61
62  MEAN = mean(SNR(:,1))
63
64
65  var = data.Station';
66  trasm_up = array2table(trasm_up);
67  trasm_up.Properties.VariableNames = var;
68  trasm_down = array2table(trasm_down);
69  trasm_down.Properties.VariableNames = var;
70  trasm_tot = array2table(trasm_tot);
71  trasm_tot.Properties.VariableNames = var;
72  P_return_avg = array2table(P_return_avg);
73  P_return_avg.Properties.VariableNames = var;
74  P_return_peak = array2table(P_return_peak);
75  P_return_peak.Properties.VariableNames = var;
76  SNR = array2table(SNR);
77  SNR.Properties.VariableNames = var;
78
79  angle = 90-angle;
80
81  writematrix(angle,filename,'Sheet','Power_avg_return','Range','A2')
        ;
82  writematrix(angle,filename,'Sheet','SNR','Range','A2');
83  writematrix(angle,filename,'Sheet','Trasm_tot','Range','A2');
84
85  writetable(P_return_avg,filename,'Sheet','Power_avg_return','Range'
        ,'B1');
86  writetable(SNR,filename,'Sheet','SNR','Range','B1');
87  writetable(trasm_tot,filename,'Sheet','Trasm_tot','Range','B1');
```

B.3 Visibility analysis

```matlab
1  clear
2  clc
3  filename = '3_CCR_multi.xlsx'; % Output file name
4  startTime = datetime(2027,3,30,0,0,0); % Start date and time
5  stopTime = startTime + months(1); % End time
6  sampleTime = 10; % sample time
7
8  sc = satelliteScenario(startTime,stopTime,sampleTime); % Create
       scenario
9
10 % Orbital parameters
11 a = 6871000;
12 ecc = 0;
13 incl = 96;
14 omega = 0;
15 argp = 0;
16 nu = 0;
17
18 CCR
19 ha = 30; % CCR FOV half angle
20 ccrfov = 2*ha; % CCR FOV
21
22 sat = satellite(sc,a,ecc,incl,omega,argp,nu,"Name","Alba","
       OrbitPropagator","sgp4");
23 pointAt(sat,'nadir');
24
25 % Ground stations definition
26 % MATERA
27 GS_lat =  40.6486;
28 GS_lon = 16.7046;
29 gs_MATM = groundStation(sc,GS_lat,GS_lon,"Name","MATM","Altitude"
       ,536.9,"MinElevationAngle",20);
30
31 % POSTDAM
32 GS_lat =  52.3830;
33 GS_lon = 13.0614;
34 gs_POT3 = groundStation(sc,GS_lat,GS_lon,"Name","POT3","
       MinElevationAngle",20);
35
36 % GRAZ
37 GS_lat =  47.0671;
38 GS_lon = 15.4933;
39 gs_GRZL = groundStation(sc,GS_lat,GS_lon,"Name","GRZL","Altitude"
       ,539.4,"MinElevationAngle",5);
40
41 % WETTZELL
42 GS_lat =  49.1444;
43 GS_lon = 12.8780;
44 gs_WETL = groundStation(sc,GS_lat,GS_lon,"Name","WETL","
       MinElevationAngle",20);
45
```

```matlab
46 % GRASSE
47 GS_lat =   43.7546;
48 GS_lon = 6.9216;
49 gs_GRSM = groundStation(sc,GS_lat,GS_lon,"Name","GRSM","Altitude"
      ,1323.1,"MinElevationAngle",5);
50
51 % SFERNANDO
52 GS_lat =   36.4650;
53 GS_lon = -6.2055;
54 gs_SFEL = groundStation(sc,GS_lat,GS_lon,"Name","SFEL","
      MinElevationAngle",9);
55
56 % BOROWIEC
57 GS_lat =   52.2770;
58 GS_lon = 17.0746;
59 gs_BORL = groundStation(sc,GS_lat,GS_lon,"Name","BORL","
      MinElevationAngle",20);
60
61 % ZIMMERWALD
62 GS_lat =   46.8772;
63 GS_lon = 7.4652;
64 gs_ZIML = groundStation(sc,GS_lat,GS_lon,"Name","ZIML","Altitude"
      ,951.2,"MinElevationAngle",20);
65
66 % IZANA
67 GS_lat =   28.29959791;
68 GS_lon = 16.51061160;
69 gs_IZ1L = groundStation(sc,GS_lat,GS_lon,"Name","IZ1L","Altitude"
      ,2429.7,"MinElevationAngle",20);
70
71 % HERSTMONCEUX
72 GS_lat =   50.8674;
73 GS_lon = 0.3361;
74 gs_HERL = groundStation(sc,GS_lat,GS_lon,"Name","HERL","
      MinElevationAngle",25);
75
76 % SIMOSATO
77 GS_lat =   33.5777;
78 GS_lon = 135.9370;
79 gs_SISL = groundStation(sc,GS_lat,GS_lon,"Name","SISL","
      MinElevationAngle",13);
80
81 % MT STROMLO
82 GS_lat =   -35.3161;
83 GS_lon = 149.0099;
84 gs_STL3 = groundStation(sc,GS_lat,GS_lon,"Name","STL3","
      MinElevationAngle",15);
85
86 % SHANGAI
87 GS_lat =   31.0961;
88 GS_lon = 121.1866;
89 gs_SHA2 = groundStation(sc,GS_lat,GS_lon,"Name","SHA2","
      MinElevationAngle",5);
90
91 % KUNMING
92 GS_lat =   25.0298;
```

```matlab
 93 GS_lon = 102.7977;
 94 gs_KUN2 = groundStation(sc,GS_lat,GS_lon,"Name","KUN2","Altitude"
       ,1987.05,"MinElevationAngle",10);
 95
 96 % HRTL
 97 GS_lat =  -25.889194;
 98 GS_lon = 27.6861111;
 99 gs_HRTL = groundStation(sc,GS_lat,GS_lon,"Name","HRTL","
       MinElevationAngle",20);
100
101 % HARL
102 GS_lat =  -25.8897;
103 GS_lon = 27.6861;
104 gs_HARL = groundStation(sc,GS_lat,GS_lon,"Name","HARL","Altitude"
       ,1406.8,"MinElevationAngle",20);
105
106 % BRAL
107 GS_lat =  -15.7731;
108 GS_lon = -47.8653;
109 gs_BRAL = groundStation(sc,GS_lat,GS_lon,"Name","BRAL","Altitude"
       ,1029.2,"MinElevationAngle",20);
110
111 % SJUL
112 GS_lat =  -31.5086249;
113 GS_lon = -68.6231602;
114 gs_SJUL = groundStation(sc,GS_lat,GS_lon,"Name","SJUL","
       MinElevationAngle",10);
115
116 % AREL
117 GS_lat = -16.4657;
118 GS_lon = -71.4930;
119 gs_AREL = groundStation(sc,GS_lat,GS_lon,"Name","AREL","Altitude"
       ,2489,"MinElevationAngle",20);
120
121 % JFNL
122 GS_lat =  30.515667;
123 GS_lon = 114.490167;
124 gs_JFNL = groundStation(sc,GS_lat,GS_lon,"Name","JFNL","
       MinElevationAngle",5);
125
126 % SEJL
127 GS_lat =  36.520991;
128 GS_lon = 127.302913;
129 gs_SEJL = groundStation(sc,GS_lat,GS_lon,"Name","SEJL","
       MinElevationAngle",20);
130
131 % GMSL
132 GS_lat =  30.556509654;
133 GS_lon = 131.01541710;
134 gs_GMSL = groundStation(sc,GS_lat,GS_lon,"Name","GMSL","
       MinElevationAngle",20);
135
136 % BEIL
137 GS_lat =  39.6069;
138 GS_lon = 116.8920;
139 gs_BEIL = groundStation(sc,GS_lat,GS_lon,"Name","BEIL","
```

```
          MinElevationAngle",0);
140
141  % THTL
142  GS_lat =   -17.5768;
143  GS_lon = 210.3937;
144  gs_THTL = groundStation(sc,GS_lat,GS_lon,"Name","THTL","
          MinElevationAngle",20);
145
146  % HA4T
147  GS_lat =   20.706489;
148  GS_lon = 203.743049;
149  gs_HA4T = groundStation(sc,GS_lat,GS_lon,"Name","HA4T","Altitude"
          ,3056.2,"MinElevationAngle",20);
150
151  % MONL
152  GS_lat = 32.8917;
153  GS_lon = -116.4227;
154  gs_MONL = groundStation(sc,GS_lat,GS_lon,"Name","MONL","Altitude"
          ,1842.1,"MinElevationAngle",20);
155
156  % GODL
157  GS_lat =   39.0206;
158  GS_lon = -76.82770;
159  gs_GODL = groundStation(sc,GS_lat,GS_lon,"Name","GODL","
          MinElevationAngle",10);
160
161  % YARL
162  GS_lat =   -29.0464;
163  GS_lon = 115.3467;
164  gs_YARL = groundStation(sc,GS_lat,GS_lon,"Name","YARL","
          MinElevationAngle",10);
165
166  % KTZL
167  GS_lat =   44.3932;
168  GS_lon = 33.9701;
169  gs_KTZL = groundStation(sc,GS_lat,GS_lon,"Name","KTZL","
          MinElevationAngle",20);
170
171  % IRKL
172  GS_lat = 52.2191;
173  GS_lon = 104.3164;
174  gs_IRKL = groundStation(sc,GS_lat,GS_lon,"Name","IRKL","
          MinElevationAngle",20);
175
176  % BADL
177  GS_lat = 51.7700;
178  GS_lon = 102.2354;
179  gs_BADL = groundStation(sc,GS_lat,GS_lon,"Name","BADL","
          MinElevationAngle",20);
180
181  % ZELL
182  GS_lat = 43.7887;
183  GS_lon = 41.5654;
184  gs_ZELL = groundStation(sc,GS_lat,GS_lon,"Name","ZELL","Altitude"
          ,1155.4,"MinElevationAngle",20);
185
```

```
186  % SVEL
187  GS_lat =  60.5332;
188  GS_lon = 29.7805;
189  gs_SVEL = groundStation(sc,GS_lat,GS_lon,"Name","SVEL","
        MinElevationAngle",20);
190
191  % BAIL
192  GS_lat = 45.7047;
193  GS_lon = 63.3422;
194  gs_BAIL = groundStation(sc,GS_lat,GS_lon,"Name","BAIL","
        MinElevationAngle",20);
195
196  % ARKL
197  GS_lat =  43.6500;
198  GS_lon = 41.4333;
199  gs_ARKL = groundStation(sc,GS_lat,GS_lon,"Name","ARKL","Altitude"
        ,2077,"MinElevationAngle",0);
200
201  % RIGL
202  GS_lat = 56.948551;
203  GS_lon = 24.059075;
204  gs_RIGL = groundStation(sc,GS_lat,GS_lon,"Name","RIGL","
        MinElevationAngle",15);
205
206  % ALTL
207  GS_lat =  51.2;
208  GS_lon = 82.3;
209  gs_ALTL = groundStation(sc,GS_lat,GS_lon,"Name","ALTL","
        MinElevationAngle",20);
210
211  % MDVS
212  GS_lat = 56.027736;
213  GS_lon = 37.224903;
214  gs_MDVS = groundStation(sc,GS_lat,GS_lon,"Name","MDVS","
        MinElevationAngle",20);
215
216  % SIML
217  GS_lat =  44.4128;
218  GS_lon = 33.9931;
219  gs_SIML = groundStation(sc,GS_lat,GS_lon,"Name","SIML","
        MinElevationAngle",12);
220
221
222  % CCRs definition
223  conicalSensor(sat,"Name","+Y","MaxViewAngle",ccrfov,"MountingAngle"
        ,[90 i_ccr 0]);
224  conicalSensor(sat,"Name","-Y","MaxViewAngle",ccrfov,"MountingAngle"
        ,[270 i_ccr 0]);
225  conicalSensor(sat,"Name","+Z","MaxViewAngle",ccrfov);
226  cam = [sat.ConicalSensors];
227
228  % CCR visibility assessment
229  for idx = 1:numel(cam)
230      access(cam(idx),gs_MAT);
231      access(cam(idx),gs_PSD);
232      access(cam(idx),gs_GRZ);
```

```matlab
233        access ( cam ( idx ) , gs_WETL );
234        access ( cam ( idx ) , gs_GRSM );
235        access ( cam ( idx ) , gs_SFEL );
236        access ( cam ( idx ) , gs_BORL );
237        access ( cam ( idx ) , gs_ZIML );
238        access ( cam ( idx ) , gs_IZ1L );
239 end
240
241 % CCR visibility table
242 ac = [ cam . Accesses ];
243 accessTable = accessIntervals ( ac );
244 accessTable = sortrows ( accessTable , 'StartTime' , 'ascend' );
245
246 % Whole CCR array analysis
247 for idx = 1: numel ( ac )
248     [s , time ] = accessStatus ( ac ( idx ));
249
250     if idx == 1
251         systemWideAccessStatus = s;
252     else
253         systemWideAccessStatus = or ( systemWideAccessStatus , s );
254     end
255 end
256
257 plot ( time , systemWideAccessStatus , "LineWidth" ,2);
258 grid on;
259 xlabel ( "Time" );
260 ylabel ( "System - Wide Access Status" );
261
262 % Total visibility duration and percentage
263 n = nnz ( systemWideAccessStatus );
264 systemWideAccessDuration = n * sc . SampleTime
265 scenarioDuration = seconds ( sc . StopTime - sc . StartTime );
266 systemWideAccessPercentage = ( systemWideAccessDuration /
        scenarioDuration ) *100
267
268 % Group passes
269 s_db = double ( systemWideAccessStatus );
270 start1 = strfind ([0 , s_db ==1] ,[0 1]);
271 end1 = strfind ([ s_db ==1 ,0] ,[1 0]);
272 Duration = end1 - start1 + 1;
273 Duration = ( Duration * sampleTime ) - sampleTime ;
274 Duration = seconds ( Duration );
275 Duration . Format = 'mm:ss ';
276 Duration = Duration ';
277 StartTime = time ( start1 ) ';
278 EndTime = time ( end1 ) ';
279 AccessTable = table ( StartTime , EndTime , Duration );
280
281 bar ( StartTime , Duration ,1)
282
283 Max = max ( Duration )
284 Min = min ( Duration )
285 Mean = mean ( Duration )
286
287 T= table ( systemWideAccessDuration , systemWideAccessPercentage , Max , Min
```

```
        , Mean ) ;
288
289 % Write Excel output file
290 writetable ( AccessTable , filename , 'Sheet' , 'Riepilogo' , 'Range' , 'A1' ) ;
291 writetable ( accessTable , filename , 'Sheet' , 'Dettaglio' , 'Range' , 'A1' ) ;
292 writetable (T , filename , 'Sheet' , 'Riepilogo' , 'Range' , 'F1' ) ;
293
294 % View scenario
295 v = satelliteScenarioViewer ( sc ) ;
296 fov = fieldOfView ( cam , "LineColor" , 'g' ) ;
```

B.4 Attitude determination accuracy assessment

```
1 clear
2 clc
3 close all
4
5 startTime = datetime (2027 ,3 ,30 ,23 ,0 ,30) ;
6 stopTime = startTime + seconds (80) ;
7 sampleTime = 0.01;
8
9 sc = satelliteScenario ( startTime , stopTime , sampleTime ) ;
10
11 % Orbital parameters
12 a = 6871000;
13 ecc = 0;
14 incl = 96;
15 omega = 2;
16 argp = 0;
17 nu = 130;
18
19 % CCR FOV
20 ha = 30;
21 ccrfov = 2*ha;
22
23 % Create satellite object with nadir pointing attitude
24 sat = satellite ( sc ,a , ecc , incl , omega , argp ,nu , "Name" , "Alba" , "
    OrbitPropagator" , "sgp4" ) ;
25 pointAt ( sat , attitude , 'CoordinateFrame' , 'ned' , 'Format' , 'quaternion' )
    ;
26
27 % GS
28 % GRAZ
29 GS_lat =  47.0671;
30 GS_lon = 15.4933;
31 gs_GRZL = groundStation ( sc , GS_lat , GS_lon , "Name" , "GRZL" , "Altitude"
    ,539.4 , "MinElevationAngle" ,5) ;
32
33 % CCR definition
34 conicalSensor ( sat , "Name" , "CCR1" , "MaxViewAngle" , ccrfov , "
    MountingLocation" ,[0.035 0.035 0.1]) ;
```

```
35  conicalSensor(sat,"Name","CCR2","MaxViewAngle",ccrfov,"
        MountingLocation",[-0.035 0.035 0.1]);
36  conicalSensor(sat,"Name","CCR3","MaxViewAngle",ccrfov,"
        MountingLocation",[0.035 -0.035 0.1]);
37  conicalSensor(sat,"Name","CCR4","MaxViewAngle",ccrfov,"
        MountingLocation",[-0.035 -0.035 0.1]);
38
39  CCR = [sat.ConicalSensors];
40
41  dur = stopTime-startTime;
42  dur = seconds(dur);
43  step = 1;
44
45
46  for t = startTime:seconds(0.01):stopTime
47
48      % Range measurement to CCR1
49      [azimuth,elevation,range] = aer(gs_GRZL,CCR(1),t);
50      mis_CCR1(step,1) = range;
51
52      % Range measurement to CCR2
53      [azimuth,elevation,range] = aer(gs_GRZL,CCR(2),t);
54      mis_CCR2(step,1) = range;
55
56      % Range measurement to CCR3
57      [azimuth,elevation,range] = aer(gs_GRZL,CCR(3),t);
58      mis_CCR3(step,1) = range;
59
60      % Range measurement to CCR4
61      [azimuth,elevation,range] = aer(gs_GRZL,CCR(4),t);
62      mis_CCR4(step,1) = range;
63
64      % Add measure error
65      CCR1_error(step,1) = mis_CCR1(step,1) + 0.0025*randn(1);
66      CCR2_error(step,1) = mis_CCR2(step,1) + 0.0025*randn(1);
67      CCR3_error(step,1) = mis_CCR3(step,1) + 0.0025*randn(1);
68      CCR4_error(step,1) = mis_CCR4(step,1) + 0.0025*randn(1);
69
70      % Calculate real angles
71      mean_24(step,:) = [mis_CCR2(step,1) mis_CCR4(step,1)];
72      mean_24(step,1) = mean(mean_24(step,:));
73      mean_13(step,:) = [mis_CCR1(step,1) mis_CCR3(step,1)];
74      mean_13(step,1) = mean(mean_13(step,:));
75      mean_12(step,:) = [mis_CCR1(step,1) mis_CCR2(step,1)];
76      mean_12(step,1) = mean(mean_12(step,:));
77      mean_34(step,:) = [mis_CCR3(step,1) mis_CCR4(step,1)];
78      mean_34(step,1) = mean(mean_34(step,:));
79      B_roll(step,1) = mean_34(step,1) - mean_12(step,1);
80      B_pitch(step,1) = mean_13(step,1) - mean_24(step,1);
81      C_pitch(step,1) = sqrt((0.07^2)-(B_pitch(step,1))^2);
82      pitch(step,1) = rad2deg(atan2(B_pitch(step,1), C_pitch(step,1))
        );
83      C_roll(step,1) = sqrt((0.07^2)-(B_roll(step,1))^2);
84      roll(step,1) = rad2deg(atan2(B_roll(step,1), C_roll(step,1)));
85  %
86      % Calculate measured angles
```

```matlab
87     mean_24_error(step,:) = [CCR2_error(step,1) CCR4_error(step,1)
       ];
88     mean_24_error(step,1) = mean(mean_24_error(step,:));
89     mean_13_error(step,:) = [CCR1_error(step,1) CCR3_error(step,1)
       ];
90     mean_13_error(step,1) = mean(mean_13_error(step,:));
91     mean_12_error(step,:) = [CCR1_error(step,1) CCR2_error(step,1)
       ];
92     mean_12_error(step,1) = mean(mean_12_error(step,:));
93     mean_34_error(step,:) = [CCR3_error(step,1) CCR4_error(step,1)
       ];
94     mean_34_error(step,1) = mean(mean_34_error(step,:));
95     B_roll_error(step,1) = mean_34_error(step,1) - mean_12_error(
       step,1);
96     B_pitch_error(step,1) = mean_13_error(step,1) - mean_24_error(
       step,1);
97     if abs(B_pitch_error(step,1))>= 0.07
98         C_pitch_error(step,1) = imag(sqrt((0.07^2)-(B_pitch_error(
       step,1))^2));
99     else
100        C_pitch_error(step,1) = sqrt((0.07^2)-(B_pitch_error(step
       ,1))^2);
101    end;
102    pitch_error(step,1) = rad2deg(atan2(B_pitch_error(step,1),
       C_pitch_error(step,1)));
103    if abs(B_roll_error(step,1))>0.07
104        C_roll_error(step,1) = imag(sqrt((0.07^2)-(B_roll_error(
       step,1))^2));
105    else
106        C_roll_error(step,1) = sqrt((0.07^2)-(B_roll_error(step,1))
       ^2);
107    end;
108
109    roll_error(step,1) = rad2deg(atan2(B_roll_error(step,1),
       C_roll_error(step,1)));
110    step = step+1;
111 end
112
113 % Delta between real and measured angles
114 delta_pitch = pitch_error-pitch;
115 delta_roll = roll_error-roll;
116
117 RMS_pitch = rms(delta_pitch)
118 RMS_roll = rms(delta_roll)
119
120 % Plot figures
121 figure(1)
122 plot(pitch_error)
123 hold on
124 plot(pitch)
125
126 figure(2)
127 plot(delta_pitch)
128
129 figure(3)
130 plot(roll_error)
```

```
131  hold on
132  plot(roll)
133
134  figure(4)
135  plot(delta_roll)
```

Bibliography

[1] S. B. Luthcke et al. The SLR Contribution to Precise Orbit Determination in the GPS Era. *13th International Workshop on Laser Ranging: Proceedings from the Science Session*, 2003.

[2] ESA Fly Your Satellite! programme. https://www.esa.int/Education/CubeSats_-_Fly_Your_Satellite/Fly_Your_Satellite!_programme.

[3] ESA Fly Your Satellite! Design Booster selection. https://www.esa.int/Education/CubeSats_-_Fly_Your_Satellite/Fly_Your_Satellite!_Design_Booster_pilot_selects_CubeSat_teams.

[4] ESA Fly Your Satellite! Design Booster phases. https://www.esa.int/Education/CubeSats_-_Fly_Your_Satellite/FYS_Design_Booster_phases.

[5] L. Combrinck. *Satellite Laser Ranging*. 2010.

[6] ILRS stations log. https://ilrs.gsfc.nasa.gov/network/stations/index.html.

[7] Krzysztof J. Sosnica. *Determination of Precise Satellite Orbits and Geodetic Parameters using Satellite Laser Ranging*. 2014.

[8] M.R. Pearlman, J.J. Degnan, and J.M. Bosworth. The International Laser Ranging Service. *NASA Goddard Space Center*, 2002.

[9] Pearlman M.R., Noll C.E., and Pavlis E.C. et al. The ILRS: approaching 20 years and planning for the future. *Journal of Geodesy 93*, 2019.

[10] J.J. Degnan. A Tutorial on Retroreflectors and Arrays for SLR. *ILRS Workshop, Frascati, Italy*, 2012.

[11] Yun He et al. Development of a 170-mm hollow corner cube retroreflector for the future lunar laser ranging. *Chinese Phys. B 27*, 2018.

[12] J.J. Degnan. Subcentimeter Satellite Laser Ranging Technology and its Applications. *Optica SLR webinar*, 2022.

[13] J.J. Degnan. Millimeter Accuracy Satellite Laser Ranging: A Review. *Contributions of Space Geodesy to Geodynamics: Technology*, 1993.

[14] J.J. Degnan. SLR2000: Eyesafe and autonomous single photoelectron satellite laser ranging at kilohertz rates. *Proceedings of SPIE - The International Society for Optical Engineering*, 1997.

[15] G. Kirchner et al. Ajisai Spin Parameter Determination Using Graz Kilohertz Satellite Laser Ranging Data. *IEEE Transactions on Geoscience and Remote Sensing, Vol. 45, No. 1*, 2007.

[16] D. Kucharski et al. Attitude and Spin Period of Space Debris Envisat Measured by Satellite Laser Ranging. *IEEE Transactions on Geoscience and Remote Sensing, Vol. 52, No. 12*, 2014.

[17] G. Kirchner and L. Grunwaldt et al. Laser Ranging to Nano-Satellites in LEO Orbits: Plans, Issues, Simulations. *18th International Workshop on Laser Ranging*, 2013.

[18] M. A. Steindhofer et al. Attitude determination of Galileo satellites using high-resolution kHz SLR. *Journal of Geodesy 93*, 2019.

[19] M. F. Barschke et al. Initial Results from the TechnoSat in-Orbit Demonstration Mission. *32nd Annual AIAA/USU Conference on Small Satellites*, 2018.

[20] ECSS Secretariat - Requirements & Standards Division. *ECSS-E-ST-10-06C – Technical requirements specification*. ESA-ESTEC, Noordwijk, The Netherlands, March 2009.

[21] A. Tomaello and C. Bonato et al. Link budget and background noise for satellite quantum key distribution. *Advances in Space Research, Volume 47, Issue 5*, 2010.

[22] MATLAB Satellite Communications Toolbox documentation : comparison of orbital propagators. https://it.mathworks.com/help/satcom/ug/comparison-of-orbit-propagators.html.

[23] Thorlabs PS977-A - TIR Retroreflector, Ø12.7 mm, L = 11.4 mm, AR Coating: 350 - 700 nm. https://www.thorlabs.com/thorproduct.cfm?partnumber=PS977-A.

[24] ISIS Deployable antenna system for 1U/3U Cube-Sats. https://www.cubesatshop.com/product/isis-deployable-antenna-system-for-1u-3u-cubesats/.

[25] NanoPower P110 Datasheet. https://gomspace.com/UserFiles/Subsystems/datasheet/gs-ds-nanopower-p110-210.pdf.